Transient wave in a transformable periodic flexural structure

Nieves, M. J.; Mishuris, G. S.; Slepyan, L. I.

Published in:
International Journal of Solids and Structures

DOI:
10.1016/j.ijsolstr.2016.11.012

Publication date:
2017

Citation for published version (APA):
Nieves, M. J., Mishuris, G. S., & Slepyan, L. I. (2017). Transient wave in a transformable periodic flexural structure. *International Journal of Solids and Structures*, *112*, 185-208. https://doi.org/10.1016/j.ijsolstr.2016.11.012

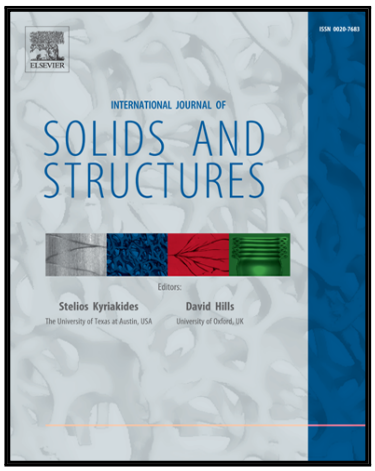

Transient wave in a transformable periodic flexural structure

M.J. Nieves, G.S. Mishuris, L.I. Slepyan

PII: S0020-7683(16)30340-7
DOI: 10.1016/j.ijsolstr.2016.11.012
Reference: SAS 9365

To appear in: *International Journal of Solids and Structures*

Received date: 15 April 2016
Revised date: 7 November 2016
Accepted date: 14 November 2016

Please cite this article as: M.J. Nieves, G.S. Mishuris, L.I. Slepyan, Transient wave in a transformable periodic flexural structure, *International Journal of Solids and Structures* (2016), doi: 10.1016/j.ijsolstr.2016.11.012

Transient wave in a transformable periodic flexural structure

M.J. Nieves[*], G.S. Mishuris[†] and L.I. Slepyan[‡]

Abstract

The analysis of a transition wave propagating in a finite heterogeneous discrete beam strip, composed of periodically placed masses and subjected to a harmonic load is presented. The load is assumed to be located sufficiently far away from the transition front. As waves propagate inside the structure, connections are broken and we investigate how this process evolves from the transient regime to the steady-state regime. It is found that the steady-state speed of this transition process, in the averaged sense, coincides with the predicted phase speed of the transition wave. For a given heterogeneity, we show that a transition wave can propagate steadily if the load amplitude and frequency are situated in a parameter subdomain. The steady-state regime does not exist outside of this domain. At a given load frequency, it is demonstrated that the average speed of fracture is independent of the load amplitude within a given steady-state domain and the number of such domains depends on the load frequency and structural heterogeneity. During the transition process, we identify several dynamic effects, including regimes where waves can be transmitted ahead of the front into the structure and the development of an inclination that follows the transition front in the steady-state regime. The occurrence of such effects and their behaviour also correspond to predictions from the theory. We show although the theoretical steady-state fracture regimes are realised globally, locally the fracture speed always behaves in a regular fashion.

1 Introduction

In contrast to the studies on mass-spring structures, to the best of the authors' knowledge dynamic transition wave propagation in beam structures has only been considered in a few articles. We refer to [7, 25] where transition wave propagation was studied in heavy supported beams and the failure phenomenon associated with the San Saba bridge was considered. In particular, in [26], several theoretical results concerning the propagation of a failure wave in an infinite beam structure, produced by a remote sinusoidal load, were obtained. The transition process is represented by the failure of members forming the supports in the

[*]Mechanical Engineering and Materials Research Centre, Liverpool John Moores University, James Parsons Building, Byrom Street, Liverpool L3 3AF, U.K.

[†]Institute of Mathematics and Physics, Aberystwyth University, Wales, U.K.

[‡]School of Mechanical Engineering, Tel Aviv University, Tel Aviv, Israel

structure and this process is assumed to propagate at a constant speed. However, those 3 papers (as we show later) do not give a complete picture of the behaviour of the transition wave propagating through these structures.

Here we present a numerical investigation of the transient problem for a failure wave propagating inside a sufficiently long finite beam structure, which brings us closer to its understanding whilst simultaneously identifying new mysteries associated with this phenomenon. In addition, we verify that the numerical approach is correct through direct comparison of the eventual steady-state behaviour with the theoretical predictions of [26]. As mentioned, we focus on the transient problem of failure propagation but it should be noted that static, quasi-static failure and fatigue processes for discrete structures can be found in [30].

Even for relatively small structures, numerical analysis of such a transition wave is computationally laborious and costly in terms of time. The solutions of such computations may have limited information and scope of applicability in understanding the general behaviour of similar structures or the same structure under different loading conditions. It is not always the case that the associated results are reliable in presenting the true physical behaviour of the damage process in a material or structure. For verification, one should use either an analytical or experimental approach, with the former being the cheapest option.

Note that the type of problem considered is important in applications to nanomaterials and in understanding fracture phenomena in continuous media on the micro-scale.

Both the finite element and boundary element method combined with the linear elastic fracture mechanics (LEFM) are useful in determining the fracture behaviour in continua. Dual boundary element methods have been used to model dynamic fracture in isotropic [11] and anisotropic [1] elastic materials. A review on the advances of the boundary element method can be found in [2]. Numerical studies of dynamic fracture began in the early 1950s, when the finite element method (FEM) was used to investigate elastic-plastic fracture in [18]. The application of FEM to 2-dimensional static and quasi-static fracture problems can also be found in [12]. Three dimensional fracture problems treated using FEM are also covered in the review [16], where a 2-dimensional dynamic fracture problem inside a loaded plate is discussed additionally. In [3], finite element models with embedded discontinuities have been proposed to model dynamic crack propagation in materials and were found to agree well with existing experimental results. The problem with using the LEFM approach is that it ignores certain information about the microscale processes involved during a crack's evolution. It also gives rise to singular stress fields at the crack tips, which in practice does not occur.

Cohesive fracture models have been used in conjunction with FEM to investigate damage propagation within different materials, for different loading scenarios in [8, 17, 29]. Such approaches are sometimes not sufficient to solve fracture problems as they are required to capture several factors involved in the actual behaviour of the material, for instance, understanding how cracks initiate, nucleate and branch [31, 41, 42]. There are also different physical phenomena occurring during the fracture process at different scales which needs to be traced [5, 20].

The microstructural influence on fracture phenomena can be traced if one uses a lattice or discrete structure, composed of masses linked by connectors [19]. This approach has been used to model a variety of problems concerning damage propagation in civil engineering structures and micro-structured material materials, known as metamaterials.

The widespread destruction of a civil engineering structure resulting from some localised

damage or external loading is known as progressive collapse [4, 15]. The avoidance of such a phenomenon is of crucial importance when structures such as buildings and bridges are designed for public use. Hence, progressive collapse of engineering structures has generated experimental, numerical and analytical studies. Civil engineering structures such as bridges can be represented by frame-like structures composed of beams that incorporate non-linear plasticity effects at frame junctions [15]. There a sophisticated model was used that accounts for the redistribution of the loading during the failure process, which is a crucial effect in the propagation of progressive collapse. Nonlinear finite element analysis of a frame has been used to study the response of buildings, re-enforced by concrete pillars, that are subjected to seismic activity [14].

A lattice embeds different physical scales, that allows one to capture local fracture processes [19]. Analytical models for frame-like structures also appear in the analysis of structured materials. Commonly composed of masses and spring connectors, these structures have been used as an analytical tool to address transition wave propagation in structured materials. These models allow for various loads and factors such as geometry and material properties to be easily embedded in the analysis. Unlike LEFM for continuous materials, a lattice produces non-singular stress fields in the vicinity of defects [36].

There exist many articles in the literature which deal with crack propagation in mass-spring lattices. A collection of such problems can be found in the monograph [36]. The first analytical results concerning this steady-state transition process in mass-spring lattices can be found in [34] and [40], where the influence of microstructure on the failure process was shown. In particular, wave radiation accompanies the crack growth and this phenomena is not present in continuous models. For Mode III cracks propagating in a homogeneous lattice, this analysis has been carried out in [34]. Propagating Mode I and II cracks in elastic in-plane problems have been addressed in [35]. In [34, 35], the method of solution involves working with the Fourier transform of governing equations (associated with the moving coordinate of the crack tip) and deriving a Wiener-Hopf equation [28] along the defect faces. It is this equation that contains information about the propagation of waves and other dynamic features of the structure during the failure process.

Recently, more advanced models for transition wave propagation in spring-mass structures have been considered. We refer to the propagation of a bridged crack [22] and the removal of a thread in a mass-spring chain in the lattice [21]. Mode I crack propagation in an anisotropic triangular elastic lattice has also been considered in [27]. Further, a transition wave propagating in nonlinear mass-spring lattice is discussed in [38], whereas in [13] this phenomenon is studied in a structure with masses having non-local interactions.

Lattice models can provide accurate information about how fast a crack can propagate under a given loading and heterogeneity of the structure [23]. For mass-spring lattices, these predictions give a good agreement with numerical simulations [24]. It has been shown that structured inhomogeneities can lead to novel properties in the energy distribution in the structure, and the creation of interesting effects such as “knife waves” that can drive defect propagation.

Non-steady crack propagation behaviour can also be revealed in simulations for transition wave propagation in finite discrete square lattices with embedded defects [24]. It is possible to trace surprising crack behaviour, for instance, as observed in Mode II crack propagation in an elastic triangular lattice where a binary crack can emerge [37]. Other non-steady failure

phenomena have been identified in [39], where the continuous model of the removal of a beam attached to an elastic foundation, is considered. The discrete analogue of this problem is considered here.

Identifying non-steady or irregular regimes for transition wave propagation is important in materials science as it can occur in conventional materials. Silicon subjected to thermal loading with a high temperature gradient [10], may produce wavy or branched cracks. Wavy cracks can also occur in rubber sheets in biaxial tensile tests [9].

Beam structures are more commonly found in physics, materials science and engineering than their spring counterparts. The analysis of the static problem of a crack within a beam-made lattice has been presented in [33]. This analysis has been generalised to brittle fracture inside a three-dimensional beam frame representing an open cell foam [32].

While a majority of articles mentioned above focus on the dynamic failure of mass-spring lattices, on the contrary, very few articles exist in the literature which focus on the dynamic fracture in discrete beam structures. Transition wave propagation inside of a discrete beam structure acted on by gravity forces has been considered in [7]. The structure can represent collapse of a bridge, whose decks and supporting columns have been modelled as beams and springs, respectively. Further, in [25], an extension of this approach was carried out to model the propagation of a transition wave in collapse of the San Saba bridge, Central Texas, in 2013.

The work of [7] appears as a special case of the analytical model considered here, and in [26]. Additionally, the problem in [7] incorporates the study of a transition wave, where spring supports in the structure behind the wave front undergo a phase transition and are left intact as the transition wave propagates. Here, we consider supports which break inside the structure as a result of the action of a transition wave, and such members produce no contribution to the governing equations in the broken region. The study of steady-state fracture and phase transition in structured elastic media has been dealt with in detail in the papers [5, 20, 34, 35, 40]. Further, the propagation of a steady-state wave in structure composed of a beam resting on periodic supports has been analysed in [6, 7] in the connection to real life disasters and the collapse of civil engineering structures such as bridges and long pipeline systems.

The aim of the paper is to expand the results known for steady-state transition wave propagation in spring structures to beam structures. Theoretically, this was carried out in [26] and, as usual, from this analysis it is not straight-forward to conclude whether predicted steady-state regimes are realised. This is a problem which can be treated both experimentally and numerically, and we choose the latter approach here, where the transient model of a failure wave propagating inside a finite beam structure is considered. In particular, we verify the numerical approach here by comparing with the theoretical analysis of [26]. Simultaneously, we demonstrate the theory contains all the necessary information to accurately predict when the steady-state fracture regime can be observed in the simulations. On the other hand, as we will see, there is much more information that can be extracted from the numerical experiments which also complement the theoretical findings.

It should be noted that in [26], the solution to the problem of failure wave propagating steadily inside an infinite discrete structure was solved under the assumption that the steady-state regime exists. Moreover, the analysis for this was reduced to a problem for a function of a single variable, which describes the displacement of masses as a function of the moving

coordinate of the transition front. In contrast, here we numerically treat a similar situation inside the finite beam structure, but the displacements of the masses are treated as functions of both the spatial variable and time. The latter scenario incorporates both the transient and steady-state regimes of the transition wave, including how the transient regime reaches the steady-state regime.

The structure of the article is as follows. In section 2, the problem formulation, solution and associated results are given for a transition wave propagating inside an infinite heterogeneous strip composed of periodically placed masses connected by beams. There, the failure process is assumed to be driven by a feeding wave incident on the transition front.

In section 3, we investigate the connection between the analytical model presented in section 2 and the numerical model for the finite heterogeneous strip subjected to a sinusoidal remote load. The computational window for the transient problem is described in section 3.1 and the methods used to trace the transition front velocity is presented in section 3.2. In addition, using results stated in section 2, we formally link the solution of the analytical model of [26] to the problem of an oscillating point force inside an infinite mass-beam chain in section 3.3. We establish the method used for predicting possible steady-state speeds using the dispersive features of the infinite structure in section 3.4. The relationship between the failure criteria implemented in the numerical model and the analytical model of section 2 is shown in section 3.5. Also presented there is the description how to identify the load amplitude intervals capable of producing the steady-state regimes. We describe how the steady-state dynamic properties of the finite structure, undergoing action from the transition wave, are traced in section 3.6.

In section 4, we present the analysis of the transient problem of a failure wave propagating inside a finite discrete beam strip under a harmonic load. There we show the behaviour of the transient regime for the failure wave and how this converges to the steady-state regime. In particular, according to the approach presented in section 3, we demonstrate the accuracy of the numerical scheme by direct comparison with the theoretical results of section 2. This is carried out for various load frequencies and choices of the heterogeneity parameter. In particular, in section 4 we show in the simulations the dependency of the speed of the transition wave on the load amplitude and identify when and what theoretical steady-state regimes are realised. Finally, conclusions are then given in section 5.

2 Problem formulation for infinite beam structure

We consider the heterogeneous lattice beam strip in Figure 1, as in [26]. We do not present the full details of the results in [26] but we supply enough to enable one to understand the current study in this article. Inside the structure, point masses of mass M are arranged along the central axis periodically so that their positions are given as $x' = am$, $m \in \mathbb{Z}$. Emanating from each mass in the horizontal and vertical directions are beams of length a. Horizontal (transverse) beams have Young's modulus E_1 (E_2), and second moment of area I_1 (I_2).

The m^{th} mass has a displacement $w_m(t)$ perpendicular to the $x'y$-plane and a rotation $\theta_m^x(t)$ about an axis parallel to the transverse beams. Due to symmetry of the structure, the rotation $\theta_m^y(t)$ of the m^{th} mass about the central axis $y = 0$ is zero.

The local coordinate of the m^{th} longitudinal beam is defined as $x' = x + am$ where $0 <$

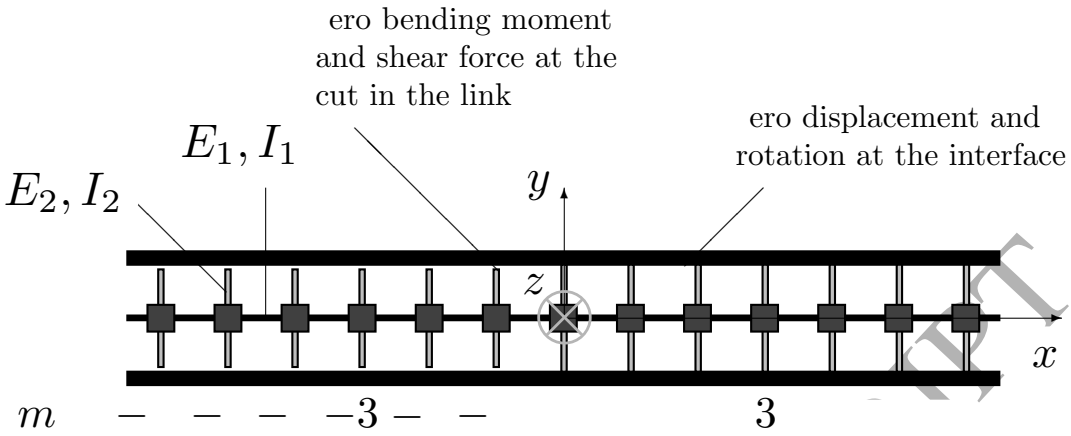

Figure 1: A heterogeneous discrete structure composed massless beams members of length a with concentrated masses M at the nodes $m \in \mathbb{Z}$. Members aligned with the horizontal (vertical) axis have Young's modulus E_1 (E_2) and second moment of area I_1 (I_2),

$x < a$. Using this coordinate, we can introduce the bending moment and shear force inside the m^{th} longitudinal beam by $\mathcal{M}_m^x(x,t)$ and $\mathcal{V}_m^x(x,t)$, respectively. The shear force $\mathcal{V}_m^y(y,t)$ inside the m^{th} transverse beam, is defined relative to the local coordinate y, $0 < y < a$.

In Figure 1, we show the case when there is an interface located at $m = 0$, separating intact and broken sections of the lattice strip. In the intact part of the strip, the transverse beams connect to a rigid interface above and below the masses, whereas in the damaged structure the transverse beams are broken at the interface. In the problem to be considered, a remote force supplies energy to the entire structure from the far left. As a result, the interface propagates steadily with a constant speed V and the associated inequalities $m \geq Vt/a$ and $m < Vt/a$ will determine the intact region and broken regions, respectively. This process defines a transition wave which propagates steadily with speed V inside the infinite structure.

The nodes within the intact region are assumed to satisfy

$$w_m(t) \leq w_c \text{ for } m = Vt/a \,, \tag{1}$$

$$w_c > w_m(t) \text{ for } m > Vt/a \,, \tag{2}$$

where w_c represents the value of critical displacement for any node inside the intact structure. When this is reached, it is assumed the transverse links at the interface break and the interface moves a units to the right inside the structure. As the transition process occurs steadily, the time between each breakage of a pair of transverse beams is a/V. The preceding criteria are necessary and sufficient to ensure the front propagates steadily through the structure. If these conditions are violated, then the transition process will propagate non-steadily in the intact structure. We note that this formulation does not allow one to determine how and whether the steady-state propagation of the transition wave is reached. In order to trace this phenomena, the full transient problem must be studied and this is the subject of investigation later inside a finite beam structure.

2.0.1 Governing equations

The governing equations for the m^{th} mass, $m \in \mathbb{Z}$, are derived by balancing forces and moments acting on this mass, to yield

$$\mathcal{V}_m^x(0,t) - \mathcal{V}_{m-1}^x(a,t) + (\mathcal{V}_m^{y,\text{top}}(0,t) - \mathcal{V}_m^{y,\text{bottom}}(a,t))H(m - Vt/a) - M\frac{\mathrm{d}^2 w_m(t)}{\mathrm{d}t^2} = 0\,, \quad (3)$$

and

$$\mathcal{M}_m^x(0,t) - \mathcal{M}_{m-1}^x(a,t) = 0\,, \quad (4)$$

respectively, where M is the mass at the m^{th} junction and we assume the moment of inertia of each mass is negligible. Here, $H(x)$ is the Heaviside function:

$$H(x) = \begin{cases} 1\,, & \text{if } x \geq 0\,, \\ 0\,, & \text{otherwise}\,. \end{cases}$$

As shown in [26], equations (3) and (4) can be completely rewritten in terms of the displacements w_m and rotations θ_m^x. Moreover, the rotations can be defined via the displacements. We invoke the moving coordinate $\eta = m - Vt/a$ in the dependencies of the displacements w_m and θ_m^x, i.e. we assume

$$w_m(t) = w(\eta)\,, \quad \theta_m^x(t) = \theta^x(\eta)\,.$$

From this point we can reduce the considered problem to one concerning a function of a single variable η (see section 2.0.2). In the numerical investigation tackled later, we return to the assumption that the displacements and rotations of each mass are both functions of the x and t in order to study the full transient problem.

The problem (3) and (4) can then be written as

$$6\left\{2[2w(\eta) - w(\eta-1) - w(\eta+1)] + a[\theta^x(\eta+1) - \theta^x(\eta-1)]\right\} + 24rw(\eta)H(\eta) + v^2\frac{\mathrm{d}^2 w(\eta)}{\mathrm{d}\eta^2} = 0\,, \quad (5)$$

and

$$3[w(\eta+1) - w(\eta-1)] - a[\theta^x(\eta+1) + \theta^x(\eta-1) + 4\theta^x(\eta)] = 0\,, \quad (6)$$

where

$$r = \frac{E_2 I_2}{E_1 I_1}, \quad \text{and} \quad v = \sqrt{\frac{Ma}{E_1 I_1}}V\,.$$

Here r governs the heterogeneity of the structure and v is the normalised transition wave speed, respectively.

We note that due to the symmetry of the beam structure we arrive at a set of governing equations, closely linked to those presented in [7], where the propagation of a transition wave through a structure composed of a beam resting on spring supports is considered.

In the approach of [26], a feeding wave w_f incident on the transition front from the far left drives transition process, which also depends on η:

$$w_f(\eta) = A\cos(p_v\eta - \phi)\,. \quad (7)$$

Here A is the speed dependent amplitude defined relative to the transition front, p_v is the feeding wavenumber and ϕ is the wave's phase shift.

In connection with (1) and (2), for the first node in the intact structure to reach the critical displacement w_c we impose that

$$w(\eta) = w_c \quad \text{when } \eta = 0 \quad \text{and} \quad w'(\eta) < 0\ , \ \text{when } \eta \to +0\ .$$

2.0.2 Solution of the problem using the Wiener-Hopf technique

In this section, we present a summary of the solution to the problem considered in [26], which will provide the reader with sufficient information to understand the subsequent comparison between the analytical results and numerical analysis.

After the Fourier transform with respect to η, (6) gives

$$\theta^{x\mathrm{F}} = -\frac{3\mathrm{i}\sin k}{2+\cos k} w^{\mathrm{F}} \tag{8}$$

and then the equations (5) and (6) can be reduced to a single homogeneous Wiener-Hopf equation in the form

$$g_1(k)w_+(k) + g_2(k)w_-(k) = 0\ , \tag{9}$$

with $w_\pm$ connected with the Fourier transforms:

$$\{w^{\mathrm{F}}, \theta^{x\mathrm{F}}\} = \int_{-\infty}^{\infty} \{w(\eta), \theta^x(\eta)\} e^{\mathrm{i}k\eta} d\eta\ , \qquad w_\pm(k) = \int_{-\infty}^{\infty} w(\eta) e^{\mathrm{i}k\eta} H(\pm\eta) d\eta\ ,$$

and

$$g_1(k) = \frac{12(1-\cos k)^2}{\cos k + 2} + 24r + (0 + \mathrm{i}kv)^2\ , \tag{10}$$

$$g_2(k) = g_1(k) - 24r\ . \tag{11}$$

In (10), the notation $0 + \mathrm{i}kv = \lim\limits_{\varepsilon \to +0} \varepsilon + \mathrm{i}kv$. The functions $g_j(k)$, $j = 1, 2$, determine the dispersion relations for the heterogeneous structure, which are discussed in section 2.0.3 below. In what follows, for a given transition wave speed v, we assume the points $k = +0\mathrm{i}, \pm p_{2i} + 0\mathrm{i}, \pm p_{2i-1} + 0\mathrm{i}$, $1 \le i \le n$ are zeros of the functions $g_2(k)$. Likewise, let $k = \pm q_{2i} - 0\mathrm{i}, \pm q_{2i+1} + 0\mathrm{i}$, $0 \le i \le \nu$ be the zeros of function $g_1(k)$ (note if $\nu = 0$, we consider $k = \pm q_1 + 0\mathrm{i}$ as the only pair of zeros). The parameters n and ν can be traced from the dispersion curves, which are presented in sections 2.0.3 and 3.4.

One may modify the equation (9) to incorporate the action of a remote load, relative to the transition front, in the right-hand side. Here we consider a remote vibrating load to the left of the transition front, which produces a wave incident on this point. This allows (9) to be written as

$$\frac{1}{L_+(k)\Psi_+(k)} w_+(k) + \frac{L_-(k)}{\Psi_-(k)} w_-(k) = \Phi(k)\ , \tag{12}$$

where $\Phi(k)$ reflects the action of this load and it is represented as

$$\Phi(k) \ = \ \frac{C\mathrm{e}^{\mathrm{i}\phi}}{0 + \mathrm{i}(k - p_v)} + \frac{C\mathrm{e}^{\mathrm{i}\phi}}{0 - \mathrm{i}(k - p_v)} + \frac{\overline{C}\mathrm{e}^{-\mathrm{i}\phi}}{0 + \mathrm{i}(k + p_v)} + \frac{\overline{C}\mathrm{e}^{-\mathrm{i}\phi}}{0 - \mathrm{i}(k + p_v)}\ .$$

Here p_v is the wavenumber for the feeding wave produced by the remote load and the parameter C is related to the amplitude A of the feeding wave with phase ϕ, via

$$C = \frac{L_-(p_v)}{\Psi_-(p_v)} \frac{A}{2a} \,. \tag{13}$$

In addition, $\Psi_\pm$ are meromorphic functions in (12), found in [26], that are given by

$$\Psi_+ = \frac{(1-\mathrm{i}k)^{2(\nu-n)} \prod_{j=1}^{n} (0-\mathrm{i}(k-p_{2j-1}))(0-\mathrm{i}(k+p_{2j-1}))}{\prod_{j=1}^{\nu} (0-\mathrm{i}(k-q_{2j}))(0-\mathrm{i}(k+q_{2j}))} \,, \tag{14}$$

$$\Psi_- = \frac{\prod_{j=0}^{\nu} (0+\mathrm{i}(k-q_{2j+1}))(0+\mathrm{i}(k+q_{2j+1}))}{(1+\mathrm{i}k)^{2(\nu-n)}(0+\mathrm{i}k)^2 \prod_{j=1}^{n} (0+\mathrm{i}(k-p_{2j}))(0+\mathrm{i}(k+p_{2j}))} \,,$$

and

$$L(k) = L_+(k) L_-(k) \,, \quad L_\pm(k) = \exp\left[\pm \frac{1}{2\pi\mathrm{i}} \int_{-\infty}^{\infty} \frac{\ln L(\xi)}{\xi - k} \, \mathrm{d}\xi \right] \quad (\pm \Im k > 0) \,,$$

which follows from the Cauchy factorisation of the function

$$L(k) = \frac{\Psi_-(k)}{\Psi_+(k)} \frac{g_2(k)}{g_1(k)}$$

that has no zeros or poles on the real axis and $L(k) > 0$.

Equation (12) was solved in [26] and the solution is

$$w_+(k) = L_+(k) \Psi_+(k) \left[\frac{C \mathrm{e}^{\mathrm{i}\phi}}{0 - \mathrm{i}(k-p_v)} + \frac{\overline{C} \mathrm{e}^{-\mathrm{i}\phi}}{0 - \mathrm{i}(k+p_v)} \right] \tag{15}$$

$$w_-(k) = \frac{\Psi_-(k)}{L_-(k)} \left[\frac{C \mathrm{e}^{\mathrm{i}\phi}}{0 + \mathrm{i}(k-p_v)} + \frac{\overline{C} \mathrm{e}^{-\mathrm{i}\phi}}{0 + \mathrm{i}(k+p_v)} \right] \,. \tag{16}$$

2.0.3 Dispersion relations and connection with possible fracture modes

Dispersion relations for the infinite heterogeneous structure. For the considered structure, in [26] dispersion relations were identified for both ahead and behind the transition front by considering the zeros of g_j, $j = 1, 2$, respectively, in (10) and (11). Indeed, one should substitute $\omega = kv$ in (10) and (11), set these expressions equal to zero and rearrange for ω. For the structure ahead of the transition front, one has the dispersion relation

$$\omega_1(k) = \sqrt{\frac{12(1-\cos(k))^2}{\cos(k)+2} + 24r} \tag{17}$$

where k is the dimensionless wave number and $r = E_2 I_2 / E_1 I_1$ is a contrast parameter governing the heterogeneity of the structure.

Behind the transition front, the existence of waves propagating in this region is determined by

$$\omega_2(k) = \sqrt{\frac{12(1-\cos(k))^2}{\cos(k)+2}} \,. \tag{18}$$

Zeros of the functions $g_1(k)$ ***and*** $g_2(k)$**.** The dispersion relations (17) and (18) are shown in Figure 2. Given a transition front speed v, existence of waves ahead and behind this point are then determined by analysing the intersection points of the ray $\omega = kv$ with the corresponding dispersion curves. Such intersections correspond to the zeros of the functions g_j, $j = 1, 2$. The zeros are arranged as follows.

At each intersection point with ω_j the velocity v should be compared with the group velocity $v_g = \frac{\mathrm{d}\omega_j(k)}{\mathrm{d}k}$, $j = 1, 2$. The function $g_2(k)$ has a double zero at $k = 0$, in addition to one or more pairs of non-trivial zeros $k = \pm p_1, \ldots, \pm p_{2n}$. Here the integer $n > 0$ can change according to v. At intersection points corresponding to

1. $k = p_{2j-1}$, $j = 1, \ldots, n$ we have $v < v_g$,
2. whereas for $k = 0, p_{2n}$, $j = 1, \ldots, n$, we have $v > v_g$.

Similarly, the function $g_2(k)$ has one, three or more pairs on non-trivial zeros at $k = \pm q_1, \ldots, q_{2\nu+1}$, where the integer $\nu \geq 0$. Intersection points corresponding to

1. $k = q_{2j+1}$, $j = 0, \ldots, \nu$ we have $v > v_g$,
2. and for $k = q_{2n}$, $j = 1, \ldots, \nu$, we have $v < v_g$.

Note the intersection points where $v > v_g$ ($v < v_g$), according to [36], are located in the upper (lower) half of the complex plane after introduction of the small parameter $\varepsilon \to +0$.

An example of a particular arrangement of p_j, $1 \leq j \leq 2n$ and q_i, $1 \leq i \leq 2\nu + 1$ is shown in the dispersion diagram of Figure 2 for a given v and heterogeneity r.

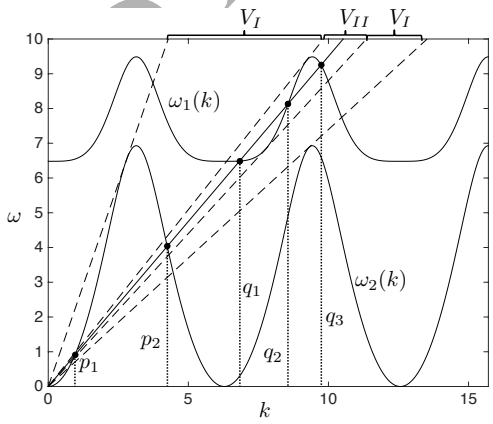

Figure 2: The dispersion diagram for the structure for $r = 1.75$. Here ω_j, $j = 1, 2$, (in (17) and (18)) are shown as functions of the normalised wavenumber k. The ray $\omega = kv$ is presented along with its intersections with ω_j, $j = 1, 2$.

General dynamic behaviour of the structure. In this section, we focus on the a particular transition front speed range $0.74 \leq v \leq 2.335$ and highlight some phenomena that can be extended to the general speed v. This is a high speed regime for the considered problem. Rays corresponding to the bounds of the transition front speed v considered here are

shown in the example of Figure 2 with dashed lines having the lowest and steepest gradients. Intersections of $\omega = kv$ with ω_j, $j = 1, 2$, corresponding to non-zero wavenumbers, imply a wave is generated with wavenumber and frequency corresponding to that intersection point.

The nonzero wavenumbers are related to waves that exist ahead of transition front (intersections of $\omega = kv$ with ω_1) and behind the transition front (intersections of $\omega = kv$ with ω_2). Here the zero wavenumber is connected with the inclination of the structure to the left of the transition front. As shown above, we compare the group velocity v_g with transition front speed at each intersection points. In this way, certain waves can be attributed to the loading of the structure. For example, a wave existing ahead (behind) of the transition front, corresponds to a wavenumber where $kv = \omega_1(k)$ ($kv = \omega_2(k)$) and if $v_g < v$ ($v_g > v$) where this condition is satisfied, this wave represents the result of the action of a load from the far right (left) of the transition front.

Failure modes. Also discussed in [26], were two special modes for the structure that can occur during the steady-state fracture process for $0.74 \leq v \leq 2.335$.

These modes are connected with the following sets for the transition front speed v:

$$\begin{aligned} V_I &:= \{v : g_1(k) = 0 \text{ for } k = \pm q_1,\, q_1 \neq 0 \} , \\ V_{II} &:= \{v : g_1(k) = 0 \text{ for } k = \pm q_j,\, 1 \leq j \leq 3,\, q_j \neq 0 \text{ and are distinct}\} . \end{aligned} \tag{19}$$

In Figure 2, we show the ray $\omega = kv$ by the solid line, for the case $v \in V_{II}$. The bounds for the set V_{II} are also indicated. In this situation, there exist non-zero wave numbers $k = \pm p_i$, $i = 1, 2$ and $k = \pm q_j$, $1 \leq j \leq 3$ for which $kv = \omega_2$ and $kv = \omega_1$, respectively. On the other hand, for $v \in V_I$, replacing $k = \pm q_j$, $1 \leq j \leq 3$, are only the wavenumbers $k = \pm q_1$.

One mode encountered admits the existence of a wave ahead of the transition front, (when $v \in V_{II}$), whereas the other does not (when $v \in V_I$). For $v \in V_I \cup V_{II}$, we also note that the structure admits a wave reflected from the transition point. This wave propagates along an inclination behind the transition front. It was shown in [26], that sets such as V_I and V_{II} can redistribute as discrete intervals of varying size for different values of the heterogeneity parameter r. In particular, if one increases v, it is possible to fluctuate between such regimes on the dispersion diagram and this effect is general for any v.

3 Connection between the numerical and analytical models

The model discussed above is considered under the assumption that the steady-state solution exists. There, no apriori knowledge of whether the steady-state regime is reached can be obtained. For this purpose, one should investigate the behaviour of the structure by studying the corresponding transient problem that assumes the displacements and rotations of masses depend on the spatial variable and time. Our goal is to answer all these questions.

In section 4, a finite heterogeneous structure subjected to a harmonic load and arranged as in Figure 1 is considered. Under certain restrictions, it is plausible to expect that the finite structure will reproduce some of the phenomena associated with the problem for the infinite structure discussed in section 2. In particular, the numerical model will show how

the transition process begins and how the transient behaviour of this phenomena settles to the steady state.

When considering the steady-state regimes identified in section 2, it is natural to ask which of the theoretically predicted steady-state regimes (note there are formally infinitely many) are realised in the transient problem and when?

To answer this question, first we must formally connect the analytical results of section 2 for an infinite heterogeneous strip subjected to the remote load to the finite structure with the sinusoidal load having a specified position. We describe the geometry of the finite structure and the form of the loading in section 3.1. We present how we compute the velocity of the transition front observed in the numerical simulations of section 3.2.

The connection between the numerical model considered and the model of section 2 is then discussed in detail in sections 3.3–3.6. As a result, we show that under restrictions on the length of the structure, the initial conditions imposed and the time taken to compute each simulation for a given load amplitude, that it is possible to observe the steady-state regimes within the transient problem that are predicted by the analytical solution for infinite heterogeneous structure. While showing such regimes exist in the numerical model for the transient problem, using the analytical model we verify a collection of main features of these regimes, such as:

i) the speed of the transition wave occurring inside the structure.

ii) the existence of waves transmitted ahead of the fracture front.

iii) the profile of the beam structure. This involves predictions of the inclination of the slope behind the transition front, along which the feeding and reflected waves propagate, and the amplitude of the waves transmitted ahead of the failure front (if they exist).

iv) the constraints on the loading parameters that produce a regime with a given speed. This provides us with parameter sub-domains defined by P and ω where steady-state regimes exists.

In doing so, we show that the numerical simulations for the transient problem of a failure wave propagating through the finite heterogeneous strip are accurate.

Thus, the comparison of features associated with the solution to (12) with the outcomes of the numerical computations is presented in detail in section 4. Prior to this, we discuss the set up for the numerical illustrations.

3.1 Numerical settings

For the numerical simulations, we consider a finite structure composed of $N = \sum_{i=1}^{3} N_i$ nodes, where the integers N_i are discussed below. As before, the nodes are assigned an integer m, $1 \leq m \leq N$. Nodes whose index m satisfy

a) $1 \leq m \leq N_1$ are inside the broken region,

b) $N_1 + 1 \leq m \leq N_1 + N_2$ are located in the intact region and

c) $N_1 + N_2 + 1 \leq m \leq N$ are subjected to damping (there are $N_3 = N - N_2 - N_1$ nodes that are damped at the right-end of the structure).

We assume initially that the structure is at rest. The form of the damping applied to the nodes with m satisfying $N_1 + N_2 + 1 \leq m \leq N$, is given by a gradual increase in the quantity $E_2 I_2$, representing the flexural rigidity of the transverse links. At the node $N_1 - d$, an oscillating point force of the form

$$F = P_0 \cos(\omega_0 t)$$

will be applied, where the force amplitude P_0 and frequency ω_0 can be written as

$$P_0 = \frac{E_1 I_1}{a^2} P \quad \text{and} \quad \omega_0 = \sqrt{\frac{E_1 I_1}{M a^3}}\omega \,, \tag{20}$$

with P and ω being dimensionless load amplitude and frequency, respectively.

We impose the conditions (1) and (2) in the simulations, by checking the displacements for those masses located in the intact region.

In the following illustrations, we take the number of lattice spacings between the left-end of the structure and the point force to be sufficiently large enough in order to guarantee that any reflections from the left-end do not interact with the point force in the considered computational time window. As a result, we will set $N_1 = 1600$, $N_2 = 1100$, $N_3 = 600$ (so that $N = 3300$) and $d = 99$.

For the considered structure, we assume that $E_1 = I_1 = 1$ for the horizontal beams. The computations presented here are carried out for two different structures, determined by the product $E_2 I_2$. In one structure $r = 0.5$ and in the other $r = 3.5$, representing two different types of anisotropy (in one case the links in the latter structure are stiffer than those in the former). This anisotropy determines the properties of the transverse links connected to the nodes with index m satisfying $N_1 + 1 \leq m \leq N_1 + N_2$. All links in the structure have length $a = 1$ and nodes have mass $M = 1$. According to (20) in what follows, $P_0 = P$ and $\omega_0 = \omega$.

The left-end of the structure is also supplied with the condition that the moment and shear force at this end are zero, so that the left-most beam behaves like the cantilever beam. On the other hand, the node at $m = N$ is fixed.

For each simulation, we computed within the time frame up to the moment when the waves reflected by the left- and right-most ends of the structure reach the transition front.

3.2 Evaluation of the velocity from the numerical model, average and instantaneous velocities

In the numerical simulations, amongst much else, we consider the average speed of the transition front as a function the normalised quantity $\mathcal{P} = Pa/w_c$. To create the average speed values, the polyfit routine in MATLAB was applied to the data recorded for the position of front as a function time, for each $\mathcal{P}$, to produce a linear regression. The gradient of this linear fit was taken as the average speed of the transition front and we denote this later by $\bar{v}$.

In addition to attempting to trace the average transition front speed, we consider the notion of the instantaneous speed v_i of the front. This is given by

$$v_i = \frac{m_i - m_{i-1}}{t_i - t_{i-1}} \qquad \text{if } i \geq 2 \, . \tag{21}$$

where t_i is the time at which breakage i occurs and m_i $(= m_i(t_i))$ is the position of that breakage. This instantaneous speed is used to give a qualitative description of the front speed during the transition process.

It is also interesting to consider the average transition front velocity, which is defined as

$$\langle v \rangle_i = \frac{m_i - m_*}{t_i - t_*} \qquad \text{if } t_i > t_* \, . \tag{22}$$

Here, m_* and t_* indicate a particular position and time of the front during its propagation, that is to be chosen. As we show below, the average transition front speed is sensitive to the choice of m_* and t_*. Both (21) and (22) are local measures for the speed and can reveal how quickly the transition process converges to the steady-state once it is initiated.

In some cases, as we will see later, it may be computationally difficult to identify the exact value of the load amplitude $\mathcal{P}$, which represents the beginning and end of a steady-state propagation regime with speed v. This happens due to the fact that near such values of $\mathcal{P}$ the data corresponding to (21) and (22) are irregularly distributed in a wide interval about the predicted speed v. The width of this distribution and the irregularity of the data decrease with time (see for example Figure 9, later) but this does not necessarily guarantee the convergence to v outside the computational window. To refine the search for the limiting values of $\mathcal{P}$, the computational window should be increased.

As the linear regression (used to recover the average transition front speed) is a global measure, the data corresponding to the instantaneous speeds and average transition front velocity (defined in (21) and (22), respectively), were used to indicate where best to apply the linear regression to the data.

Before demonstrating the numerical results and comparing these with analytical model, we should show how the results described in section 2 and [26] for the infinite heterogeneous structure can be formally connected to the structure of a finite length. To resolve this, in the next section, we relate the action of the oscillating point force inside the finite structure to the results for the propagation of a transition wave inside an infinite structure with a sinusoidal wave incident on the front.

3.3 The feeding wave generated by the point force

Here, waves generated by the remote source in the problem of section 2 are assumed to be caused by an oscillating point force far behind the transition front. We now state how this remote force (to the far left of the transition front) with amplitude P_0 and frequency ω_0 influences the behaviour of the feeding wave. The feeding wave is created as a result of the action of the point force, placed far away from the transition front. In the moving coordinate system, the force generates an outgoing wave that is incident on the transition front and this depends on the coordinate η, as in (7). The moving coordinate η can be

linked to the frequency ω_0 by $\eta = m - \omega_0 t/p_v = m - Vt/a$ (where $\omega_0 = p_v V$). Here p_v is the normalised wavenumber connected to the feeding wave.

In this case, formally the amplitude of the feeding wave A can be written in terms of P (see (20)) according to

$$A = \frac{Pa}{2p_v S_0(p_v)} \,, \tag{23}$$

where

$$S_0(k) = \frac{S(k)}{(0 - \mathrm{i}(k - p_v))(0 + \mathrm{i}(k + p_v))} \,, \quad S = \frac{48 \sin^4 k/2}{2 + \cos k} + (0 + \mathrm{i}\omega)^2 \,.$$

It should be mentioned that the right-hand side of (23) is the amplitude of the wave observed far away from the point force having amplitude P and frequency ω. The technical derivations of these results are contained below.

Derivation of the relation between feeding wave and oscillating force amplitudes. We consider here a harmonic force applied at $m = 0$ within an infinite beam structure (with no transverse supports). The equations for the balance of the shear forces and moments are

$$\frac{6E_1I_1}{a^3}\left\{2[2w_m(t) - w_{m-1}(t) - w_{m+1}(t)] + a[\theta^x_{m+1}(t) - \theta^x_{m-1}(t)]\right\} + M\frac{\mathrm{d}^2 w_m(t)}{\mathrm{d}t^2} + P_0 \mathrm{e}^{\mathrm{i}\omega_0 t}\delta_{m0} \,, = 0$$

$$3[w_{m+1}(t) - w_{m-1}(t)] - a[\theta^x_{m+1}(t) + \theta^x_{m-1}(t) + 4\theta^x_m(t)] = 0 \,,$$

where P_0 is the force amplitude, $\omega_0 = \tilde{p}_v V$, with $\tilde{p}_v$ as the wavenumber corresponding to the feeding wave ($p_v = \tilde{p}_v a$ being the dimensionless wavenumber) and V is the transition front speed ($V = \sqrt{\frac{E_1 I_1}{Ma}} v$). We employ the same normalisation for the displacement w_m as in section 3, and set $P = \frac{a^2}{E_1 I_1} P_0$ which gives

$$6\left\{2[2\tilde{w}_m(t) - \tilde{w}_{m-1}(t) - \tilde{w}_{m+1}(t)] + [\theta^x_{m+1}(t) - \theta^x_{m-1}(t)]\right\} + \frac{Ma^3}{E_1 I_1}\frac{\mathrm{d}^2 \tilde{w}_m(t)}{\mathrm{d}t^2} + P\mathrm{e}^{\mathrm{i}\omega_0 t}\delta_{m0} = 0 \,,$$

$$3[\tilde{w}_{m+1}(t) - \tilde{w}_{m-1}(t)] - [\theta^x_{m+1}(t) + \theta^x_{m-1}(t) + 4\theta^x_m(t)] = 0 \,.$$

We now omit the tilde above the displacement w, with it being understood it is now normalised. Through the normalisation $V = \sqrt{\frac{E_1 I_1}{Ma}} v$, we can set $\omega_0 = \sqrt{\frac{E_1 I_1}{Ma^3}}\omega$ with $\omega = p_v v$ being the dimensionless frequency. The equations for the forced waves can then be defined with respect to $(u_m, \zeta_m) = (w_m(t), \theta^x_m(t))\mathrm{e}^{-\mathrm{i}\omega_0 t}$ as

$$6\left\{2[2u_m - u_{m-1} - u_{m+1}] + [\zeta_{m+1} - \zeta_{m-1}]\right\} - \omega^2 u_m = -P \,,$$

$$3(u_{m+1} - u_{m-1}) - (\zeta_{m+1} + \zeta_{m-1} + 4\zeta_m) = 0 \,.$$

The discrete Fourier transform (represented by the superscript F) results in the following

$$\begin{aligned} 6[4(1-\cos k)u^F - 2\mathrm{i}\sin k\zeta^F] - \omega^2 u^F &= -P\,, \\ -6\mathrm{i}\sin k u^F - 2(2+\cos k)\zeta^F &= 0\,, \end{aligned}$$

from which it follows that

$$u^F(k) = -\frac{P}{S}\,, \quad S = \frac{48\sin^4 k/2}{2+\cos k} + (0+\mathrm{i}\omega)^2\,.$$

Referring to section 2 we see that

$$S = 0 \quad \text{at} \quad k = \pm p_v \pm \mathrm{i}0\,;$$

however, in contrast to $g_2(k)$, there are only these two zeros in the integration interval, $-\pi < k \leq \pi$

$$S = (0 - \mathrm{i}(k-k_1))(0+\mathrm{i}(k+k_1))S_0(k)\,,$$

where $S_0(k) > 0$. Finally, using the inverse transform formula we obtain the asymptotes of $\Re(w_m(t))$ as $|m| \to \infty$ (corresponding to the real external force $P_0\cos(\omega_0 t)$)

$$w_m \sim \frac{Pa}{2p_v S_0(p_v)}\cos(p_v m - \omega_0 t - \frac{\pi}{2}) \quad \text{as} \quad m \to \infty\,, \tag{24}$$

$$w_m \sim \frac{Pa}{2p_v S_0(p_v)}\cos(p_v m + \omega_0 t + \frac{\pi}{2}) \quad \text{as} \quad m \to -\infty\,.$$

Since $\eta = m - \omega_0 t/k_1 = m - Vt/a$, by comparing with the form of the incident wave in (7) with (24), we arrive at (23). We note that here the wavenumber is determined from the intersection of the horizontal line corresponding to the ω and the curve for ω_2 on the dispersion diagram (where $v_g > v$). Such an intersection point then defines the slope v of the ray $\omega = kv$, that joins the intersection point to the origin, and v represents the speed with which the transition wave propagates.

Minimum load amplitude required for steady-state propagation. Using (16), we can deduce from (23) the necessary condition on the parameters P and w_c for the steady-state solution to exist as

$$\mathcal{P} = \frac{Pa}{w_c} \geq \Lambda = \frac{2p_v|\Psi_-(p_v)|S_0(p_v)}{|L_-(p_v)|}\,. \tag{25}$$

The term Λ therefore can be linked to the minimum load required to produce a given steady-state transition front speed. In section 3.1, we verify (25) can provide an accurate estimate for such minimum load amplitudes, for a variety of frequencies.

The function Λ is plotted in Figure 3(a), as a function of the load frequency $\omega = p_v v$, for $r = 0.5j$, $1 \leq j \leq 13$. Here, $0.548 \leq \omega \leq 6.311$ and p_v corresponds with the highest possible steady-state speed predicted on the dispersion diagram, such that $0 < p_v < \pi$.

For a given value of r, the transition wave propagates with constant speed $v = \omega/p_v$ provided the ratio $\mathcal{P}$ takes its value on or above the corresponding curve for Λ in Figure

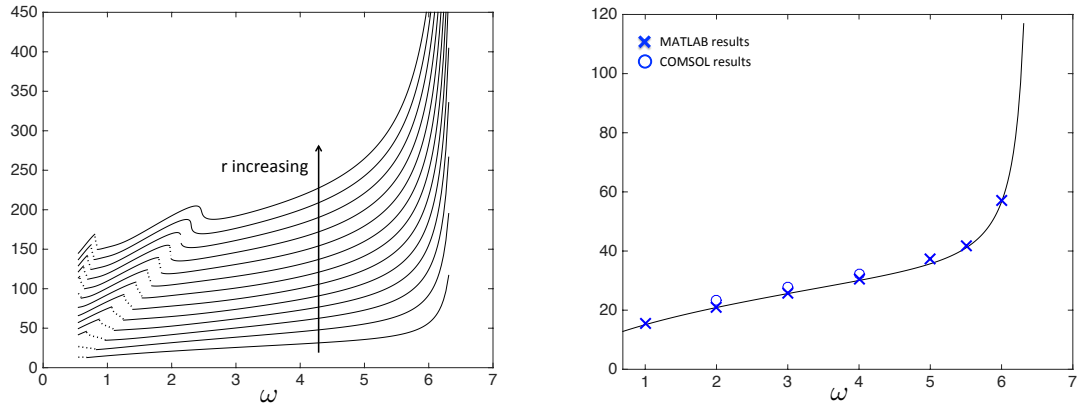

(a) (b)

Figure 3: (a) The function Λ plotted as a function of the dimensionless frequency ω for $r = 0.5j$, $1 \leq j \leq 13$. Dashed parts of each curve correspond to speeds $v = \omega/p_v \in V_{II}$ for that particular r value. (b) The quantity Λ plotted as a function of ω (solid line). For comparison, results of the numerical simulations in MATLAB and COMSOL are also given, which show the minimum value of $\mathcal{P} = Pa/w_c$ required to generate the highest steady-state speed 1.7214 of the transition front for different values of ω. It can be seen that these results give a good agreement with the theoretical prediction.

3(a). If this criterion is not satisfied, then this suggests steady-state propagation of the transition wave within the structure cannot be expected and one may observe non-steady movement of the transition front.

Figure 3(a) shows that the function Λ is monotonic for fixed ω and increasing r. For fixed r, the function Λ itself does not have a monotonic dependency on the frequency ω. The intervals connected with the speeds belonging to the set V_{II} (see (19)) are shown as dashed parts of the curves. Figure 3(a) suggests that for a certain range of the contrast parameter r, we encounter two discrete intervals for the set V_{II}, which is visible for $4 \leq r \leq 5.5$. Also note, the function Λ exhibits a singular behaviour as ω approaches its upper limit $\omega = 6.331$ (which corresponds to the speed $v = 2.335$, where we encounter a resonance point at which $v = v_g$ in Figure 2).

Comparison of Λ with results from numerical computations. Having analysed the behaviour of Λ in (25) as a function of the frequency ω, we demonstrate here the accuracy of Λ when compared with results of the simulations. We concentrate on the case $r = 0.5$ and observe the value of Λ defined in (25) as a function of the load frequency. In Figure 3(b), we plot Λ for $r = 0.5$ as a function of the load frequency $\omega = p_v v$. As an example, we take $\omega = 3$. For the considered case, Λ in (25), suggests that when $\mathcal{P} \geq \Lambda = 25.62$ the transition wave will propagate steadily (it does in fact with the speed $v = 1.7214$, as we show later). In the numerical simulations the corresponding minimum value of $\mathcal{P}$ required for this process to occur was found to be is $\mathcal{P} = \Lambda = 25.62$, which demonstrates an excellent agreement with the theoretical prediction.

In addition to the MATLAB result for $\omega = 3$, we present the results for Λ obtained

for other frequencies. It can be seen that the MATLAB results for Λ (computed with $\omega = 1, 2, 3, 4, 5, 5.5$ and 6) and in COMSOL (computed for $\omega = 2, 3, 4$) agree very well with the curve for Λ.

3.4 Dispersion relations and predicted steady-state transition wave speeds

We consider two structures for the numerical computations, corresponding to two different types of heterogeneity. We take $r = 0.5$ and 3.5. The latter value represents a structure with an intact part having stiffer transverse supports (with a higher flexural rigidity) than the former. In this case, the expected behaviour for $r = 0.5$ is that masses in the intact structure will be able to vibrate more than those contained within a stiffer structure when $r = 3.5$.

The dispersion relations (17) and (18) are presented in Figure 4, for $r = 0.5$ and 3.5. It is clear that for $r = 0.5$, in Figure 4(a), the curve corresponding to the function $\omega_1(k)$ sits on top of the curve for $\omega_2(k)$. The pass band for the intact structure is larger here than in comparison to that for $r = 3.5$ (see Figure 4(b)). There is considerable overlap between the pass bands for the intact and broken structures when $r = 0.5$, whereas no such overlap occurs for $r = 3.5$.

For $r = 0.5$, we consider the load frequencies $\omega = 0.6, 3$ and 6.25. They represent low, medium and high frequencies inside the pass band for the structure without transverse supports, defined by $0 < \omega \leq \sqrt{48} \approx 6.9282$. These frequencies are shown as horizontal lines on the dispersion diagram in Figure 4(a). We look for the intersections of such rays with the curve corresponding to $\omega_2(k)$. Each intersection point defines a ray connecting such points to the origin. The gradient of each ray supplies a prediction for the velocity v of the transition front propagation. We only consider those intersection points where $v < v_g = \mathrm{d}\omega/\,\mathrm{d}k$ and such points are shown with circles and crosses in Figures 4(a) and 4(b). Physically, these intersection points represent feeding waves with group velocity v_g capable of reaching the transition front, having speed v, and supplying energy to enable the transition process to occur. Here, in Figure 4, circles correspond to those transition front velocities which are observed in the simulations. It is clear that the number is not monotonic with respect to the increase in frequency. The crosses correspond to those states which are not observed in the subsequent numerical investigations.

Note when the ray $\omega = vp_v$ is supplied with the dispersion diagrams, one can find scenarios where more intersections of this ray with the curve for $\omega_1(k)$ occur (where $v < v_g$). This is evident from comparing Figures 4(a) and 4(b), where the pass band for the intact structure when $r = 0.5$ is larger than that for when $r = 3.5$. When $r = 0.5$, there is more opportunity to encounter such intersections, which correspond to waves that are transmitted to the structure ahead of the transition front. For $r = 3.5$ the structure ahead of the transition front behaves more like a rigid interface and hence there is less opportunity for such a phenomenon to happen.

To get a better understanding of how the predictions for the transition front speeds are obtained, we focus on the case $r = 0.5$, $\omega = 3$. In Figure 4(a), the first non-zero wavenumber corresponding to an intersection of the ray $\omega = 3$ and the dispersion curve for $\omega_2(k)$, where

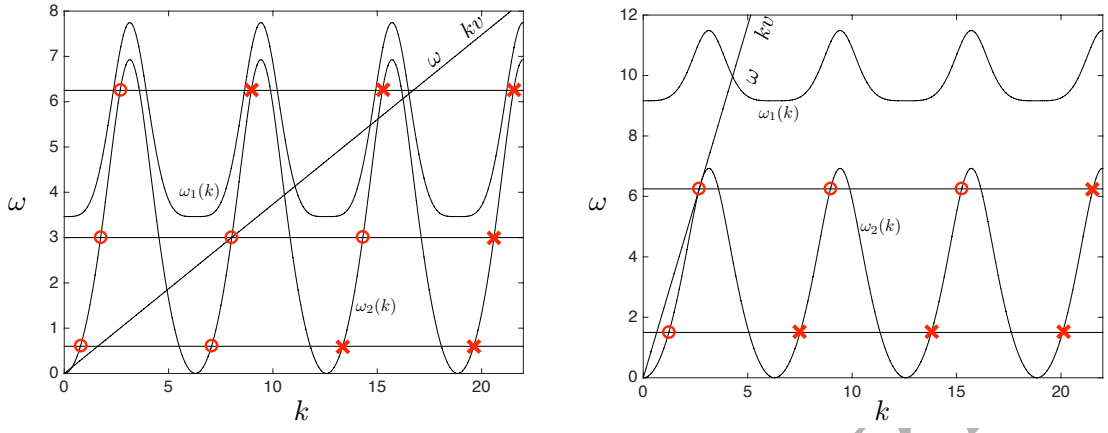

Figure 4: Dispersion relations $\omega_j(k)$, $j = 1, 2$, (see (17) and (18)) plotted as functions of k, for (a) $r = 0.5$ and (b) $r = 3.5$. Here in (a) the considered load frequencies $\omega = 0.6, 3$ and 6.25 are shown as horizontal lines. Intersection points of such lines with $\omega_2(k)$, where $v_g > v$ are indicated by either a circle or a cross. The ray $\omega = kv$ is supplied for $v = 0.3738$. In (b), similar comments hold, except $\omega = 1.5, 6.25$ and $v = 2.331$.

$v_g > v$ is approximately $k = 1.742$. The predicted transition front speed associated with this point is then computed using $v = \omega/k = 1.7214$. As the dispersion relations (17) and (18) have a periodicity of 2π, further predictions for the front speed connected with other such intersection points, can be determined through

$$v = \frac{3}{1.743 + 2\pi n}, \quad n = 0, 1, 2, 3, \ldots .$$

Below, we show that although formally the previous equation can be used to give a decreasing sequence of values for the possible average steady-state transition front speeds v, in the simulations, it is only possible to observe the first three average steady-state speeds for the chosen case.

3.5 Criterion for the steadily propagating transition wave in theoretical and numerical models

As we are concerned with the steady-state propagation of the transition front, for each simulation produced by the numerical model we check at each time step that the conditions (1) and (2) are satisfied. If these conditions are violated then the transition front will not propagate with a constant velocity. These conditions can be related to the analytical set up considered in section 2.0.1 as follows.

In the analytical model of [26], for the given load amplitude P and frequency ω $(= kv)$, the fracture criterion can be linked to the phase of the feeding wave, through

$$w_c = 2a\,\Re(Ce^{\mathrm{i}\phi}) \tag{26}$$

which comes from the consideration of (1) and C is defined by (13) and (23).

The above condition allows one to obtain a range of ϕ, the feeding wave phase, for which the steady fracture process can occur if P, ω and w_c are supplied. We note, as shown [26], that the ϕ obtained from (26), for a given P, ω and w_c, is not unique. Therefore, as discussed below, an additional condition must be supplied to determine the phase of the feeding wave observed in the transition process.

As we focus on the steady-state problem in the theoretical model, one should ensure that that no mass displacement can exceed w_c ahead of the front. Thus, as detailed in [26], it can be shown that the derivative of the solution $w(\eta)$ to the problem should satisfy

$$\lim_{\eta \to +0} w'(\eta) = 2a \left[\Re(Ce^{\mathrm{i}\phi}) \left\{ l_1 + 2(\nu - n) \right\} + p_v \Im(Ce^{\mathrm{i}\phi}) \right] < 0 \,.$$

This condition guarantees the slope of the beam along the central axis of the structure does not exceed the w_c in an immediate neighbourhood to the right of the transition front. It also allows for the unique determination of ϕ in (26).

However, a single mass ahead of the transition front can reach the critical displacment w_c. The latter scenario is in fact useful in tracing when non-steady behaviour in the transition wave can occur, as discussed in the next section.

From the analytical model we can determine the range of values for the load amplitude for when a given steady-state speed exists. Indeed, given the load frequency ω and fracture criterion w_c, one can use (25) to determine the minimum value of $\mathcal{P}$, connected with Λ (see section 3.3) for which the front propagates with speed v $(= \omega/p_v)$.

There only remains to identify the maximum value of $\mathcal{P}$ for which the same speed v is observed. For this we use the solution (15) and (16) of the Wiener-Hopf equation discussed in section 2.0.2. For a given P and ω, we compute numerically the inverse Fourier transforms of (15) and (16), together with (8), in order to identify the displacements and rotations of each mass at a given value of η. These quantities are then used to compute the beam profile using the solution of the Euler-Bernoulli equation for a massless beam.

In particular, we focus on the beam profile ahead of the point $\eta = 0$ and use the results of the inverse transform to determine the exact value of $\mathcal{P}$ for when the profile crosses the line $w(\eta) = w_c$, for $\eta > 0$. This value of $\mathcal{P}$ represents the upper bound of the range of P for which the front propagates with speed v. This together with (25) allows intervals for $\mathcal{P}$ producing steady propagation of the transition wave to be deduced.

Computations for maximum $\mathcal{P}$ for steady-state regimes. For $\omega = 3$, $r = 0.5$, Figure 5(a) shows the quantity w/w_c plotted as a function of η, with $\mathcal{P} = 330.72$. Here, $\mathcal{P} = 330.72$ represents the last value inside the interval for $\mathcal{P}$ for which the front propagates steadily with the speed 1.7214. Figure 5(a) shows a snapshot of the profile during the steady-state transition process in the numerical simulations. Recall $\eta = 0$ corresponds to the transition front.

The case discussed here corresponds to an evanescent wave propagating through the intact region, which is apparent from Figure 5(a), where $w/w_c \to 0$ as we increase η. For the discussion of when waves are transmitted to the intact structure, see section 3.6. Here we demonstrate the accuracy of the theoretical approach of [26], by supplying the computations of the displacements of the masses based on (15) (as discussed in section 3.4), which are represented by circles. A good agreement can be observed between the theoretical and numerical computations in the steady-state propagation regime.

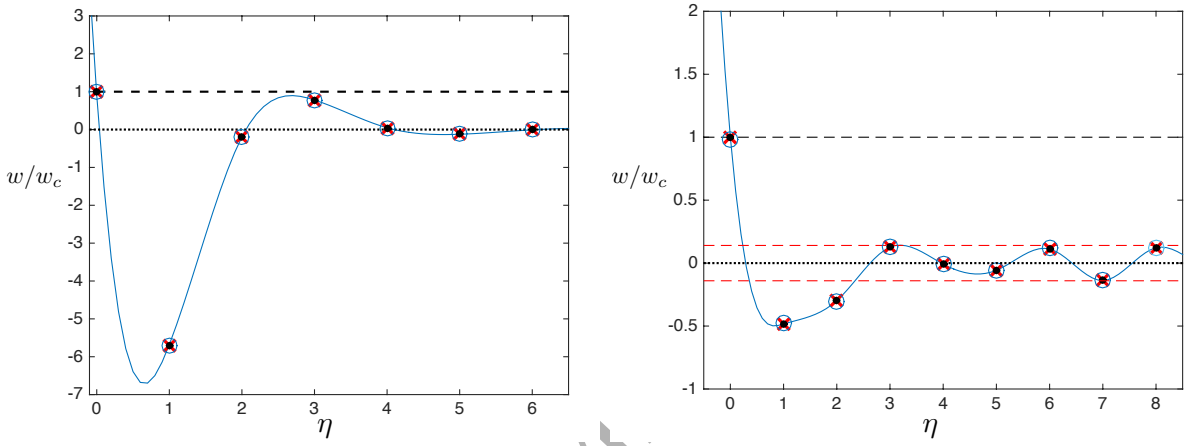

(a) (b)

Figure 5: Profiles ahead of the transition front as a function of η observed in the numerical simulations, for $r = 0.5$: (a) $\omega = 3$, and $\mathcal{P} = 330.72$, (b) $\omega = 0.6$, and $\mathcal{P} = 27.43$. The black dots with crosses indicate masses in the structure which are supported by transverse beams. In this case, the transition front propagates with the speed (a) $v = 1.7412$ and (b) $v = 0.7745$. Computations based on the solution to (12) given in [26] are shown by blue circles. They give an excellent agreement with the numerical solution during the steady-state regime. It is clearly seen in (b), as $v \in V_{II}$ (see section 2.0.3), there is a wave transmitted to ahead of the the transition front, whereas in (a) an evanescent wave is present. The prediction for the normalised amplitude A_{tr}/w_c of this wave (based on the right-hand side of (62), section 4.3.1 of [26]) is 0.1403 and this is shown with red-dashed lines.

Note for $\mathcal{P} = 330.72$, the structure exhibits a maximum occurring in Figure 5(a) at approximately $\eta = 2.75$, where $w/w_c = 0.9$. Note that $w/w_c = 1$ corresponds to the critical displacement for fracture of the transverse links, which is indicated by the dashed horizontal line. During the steady-state fracture process, the profile of the structure remains the same. The transverse links attached to nodes that reach $w/w_c = 1$ at $\eta = 0$ will break. Then the masses move along the profile so that in a time step of a/V seconds later, the positions of the masses are found in the same state shown in Figure 5(a).

Beyond $\mathcal{P} = 330.72$ the front may propagate faster than $v = 1.7214$. In fact at $\mathcal{P} = 330.75$ we see non-steady propagation of the transition front. In this situation, the maximum that occurs along the central beam of the structure for $\eta > 0$, corresponds to when $w/w_c > 1$. Transverse links connected to the masses, which move along the maximum of the profile, will break. This creates a void ahead of the transition front and a non-steady fracture pattern called forerunning fracture, discussed in [39]. Thus, in this scenario, we can assert that $\mathcal{P} = 330.72$ gives a good approximation to the upper bound for steady-state fracture propagation with a speed $v = 1.7214$.

In video 1, we show the behaviour of the finite structure for $r = 0.5$, $\omega = 3$ and $\mathcal{P} = 330.72$ in the numerical simulations. On the left of the video, we have the global view of the structure. The blue line represents the broken region and the red line is the intact part. A green frame is also present to indicate the window for the local view of the transition front on the right in the video. There, red dots indicate masses within the intact region. A horizontal dashed line is also given indicating the criterion of $w_c = 2.51$ for propagation of the transition wave in the structure. The video shows that when the displacement of the mass inside the intact structure reaches this value, the transverse links break. The red dot corresponding to that node is then removed from the structure.

Waves are generated by the point load which propagate to towards the transition front. These waves excite the masses in the vicinity of the transition front. This allows the first node in the intact region to reach the displacement w_c. Once this happens this becomes part of the broken structure and the transition process starts. Only the first node in intact region can reach the displacement w_c, and while this process occurs, displacements ahead of front begin to increase. At 00:14, a node ahead of the transition front reaches the displacement w_c and the associated transverse links break, forming a second transition front. The fracture process then oscillates between the both fronts until only one front remains. The system begins to accumulate energy to repeat the same process, which carries on up until 00:54. During this period the front accelerates. This transition process observed here is called forerunning fracture and was discovered in [39] for the continuous analogue of the problem considered here. After this, the system settles to the steady-state transition process and the transition wave propagates with the speed $v = 1.7214$. During this steady-state phase, the displacements local to the transition front take the form depicted in Figure 5(a). This case represents the steady-state fracture mode when only an evanescent wave is transmitted to the intact structure. The considered value of $\mathcal{P}$ represents the last time this steady-state regime is observed, as non-steady propagation of the transition front occurs for $\mathcal{P} > 330.72$.

We also note that past 01:00, the region behind the transition front begins to develop an inclination that follows this point (as observed in the left frame of video 1). This feature is discussed in the next section.

Video 2 demonstrates the transition process for a regime when a wave is transmitted

ahead of the front ($r = 3$, $\omega = 0.6$ and $\mathcal{P} = 27.43$). The feeding wave propagates slower than that in the case of $r = 0.5$, $\omega = 3$ and the transition process begins at 00:16. Here, no non-steady propagation of the transition front is observed, but it is clear that a wave is transmitted ahead of the transition front shown in the right window. The steady-state regime begins at 00:58, when the front begins to propagate with the speed $v = 0.7745$. The arrival of the steady-state regime is marked by the appearance of the slope following the transition front in the left window of the video.

3.6 Computations for some dynamic features of the structure

The numerical simulations discussed below, capture both the transient behaviour of the fracture process, followed by the steady-state regime. If one would like to compare results of [26] with those obtained from the computations, the simulations should run for a sufficiently long time to ensure the steady-state regime is reached and initial transient effects are negligible. Therefore, we compute up until the breakage of the 600^{th} pair of traverse links. Taking the last time instance from the simulation, we then compare the dynamic features observed with the theory of [26].

Below, attention is given to such a comparison for the waves transmitted to ahead of the transition front and the slope which follows this interface in the steady-state fracture process.

Transmitted waves in the intact structure. In the results for the last observed time step, any transmitted waves are traced by reconstructing the beam profile in a sufficiently large neighbourhood ahead of the point corresponding to $\eta = 0$. Here we will concentrate only on the case when a single wave is transmitted to ahead of the transition front.

Far from $\eta = 0$, we expect the effects of the deformation local to the transition front to be small. In this case, one should be able to observe any waves transmitted into the region $\eta > 0$. There, the amplitude of the structure's displacements will be comparable with the theoretical predictions for the amplitude of the transmitted wave A_{tr}, which is given by the right-hand side of (62) in section 4.3.1 of [26] (with $n = 1$ and $\nu = 1$). In Figure 5(b), we verify that this formula can be used to give an accurate prediction for the amplitude of the transmitted wave observed during the steady-state regime of the numerical simulation. There we show the region ahead of the transition front during steady-state transition process. Near the transition front, one can expect some local deformation. Moving further from the transition point and to the right, we retrieve a transmitted wave with amplitude indicated by the red-dashed lines.

Slope behind the transition front based on the numerical scheme. A typical comparison of the problem considered in both a static coordinate system and moving coordinate system is shown in Figure 6, where the transition front is propagating inside the the steady-state regime. These results have been taken from the numerical simulations presented in section 4 and show the general effect of variation of the load amplitude, for a given frequency. As illustrated later, there exists a slope behind the transition front along which the feeding waves and reflected waves propagate. This inclination behind the front is also predicted in the model of the infinite heterogeneous beam strip in [26]. The slope is visible in Figure 6(a), in addition to the "hill" observed between the transition front and location

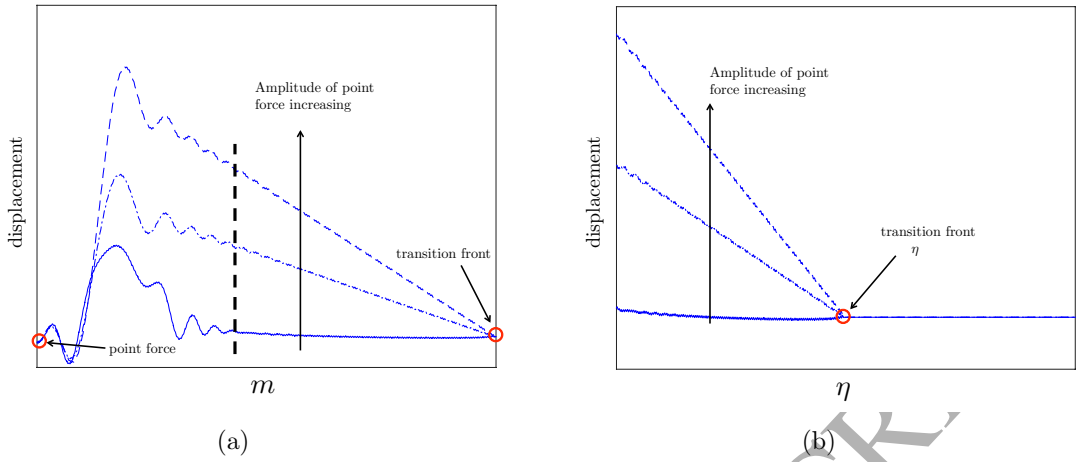

Figure 6: Example computations for the displacement of the central axis ($y = 0$) of the finite beam structure in Figure 1 as a function of (a) the index $m \in \mathbb{Z}$ and (b) η during the steady-state transition process. The example shows the effect on the change of the load amplitude, which is detailed below. To the right of the vertical dashed line in (a) the computations are shown as a function of η in (*b*).

of the point load, which appears to be an artefact of the steady-state fracture process inside the finite structure. For Figure 6(b) the same profiles are shown as a function of η, local to the transition front. In Figure 6(a), a static reference frame is given (with respect to the point force), where physical dynamic features are defined relative to this. On the other hand in (b) any physical features are defined according to η and are therefore dependent on the transition front speed v.

Slope behind the transition front based on the analytical results. In the numerical results shown here, we compute the gradient of the slope which follows the transition front from behind.

Recall that in this problem, the slope is accompanied by waves incident on and reflected from the transition front. Thus, we need to compute the gradient of the slope using a sufficiently large range of lattice points to negate effects produced by the waves and capture this gradient accurately. We apply a linear regression to the data for the slope inside the first 300 lattice units behind the transition front in the last time step of the computations.

Using the analytical model of [26], the prediction for the gradient of the slope is given as:

$$A_s = \frac{2a\,\Im(Ce^{\mathrm{i}\phi})\Psi_-^{sl}(0)}{p_v L_-(0)}\,, \tag{27}$$

where

$$\Psi_-^{sl}(k) = \frac{(-1)^{\nu-n+1}\prod_{j=0}^{\nu}(k^2-q_{2j+1}^2)}{(1+\mathrm{i}k)^{2(\nu-n)}\prod_{j=1}^{n}(k^2-p_{2j}^2)}\,, \tag{28}$$

and we compare the results from the numerical model with this.

The formulae (27) and (28) can be used to predict the inclination of the beam structure during the steady-state transition process. This is illustrated in Figure 7(a) and further

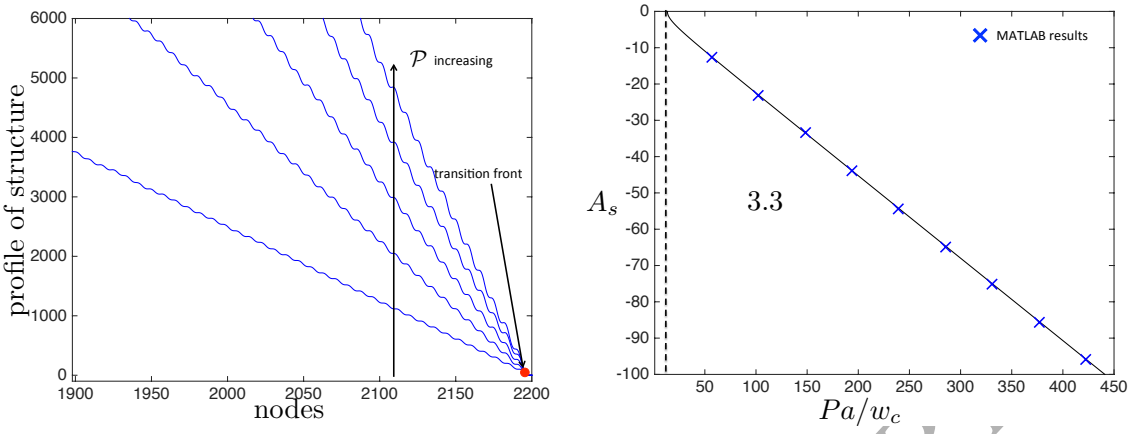

(a) (b)

Figure 7: The profile behind the transition front inside the beam structure as a function of the node number m, for $\mathcal{P} = 56.69, 102.41, 148.13, 193.86$, and 239.58. (b) The plot of (27) as a function of $\mathcal{P}$ (solid line) and corresponding MATLAB results (crosses). All figures have been produced for the parameters $\omega = 0.6$, $r = 0.5$ and $v = 0.7745$.

in section 4.1.3. For $\omega = 0.6$, $r = 0.5$, Figure 7(a) shows the inclination of the structure behind transition front observed in the numerical simulations for various load amplitudes and for a transition wave speed ($v = 0.7745$) associated with waves transmitted into the region $\eta > 0$. By performing a linear regression on the displacement profiles shown here, one can recover the inclination of this part of the structure. The comparison of these results with the computations based on the analytical prediction for A_s (with $n = 1$ and $\nu = 1$) is presented in Figure 7(b). It can be seen that the results from the simulations give an excellent agreement with the theoretical prediction (27).

4 Transient analysis for different structures and load frequencies

Now we present numerical simulations carried out in MATLAB and further demonstrate the accuracy of the numerical model by comparing with the model of section 2. Here we focus on showing the transient behaviour of the transition process in addition to analysing possible steady-state regimes when the system settles. We also consider the dependency of the steady-state regimes on the load amplitude, for various frequencies and material contrast parameter values. The case $r = 0.5$ is investigated in detail below. Following this we concentrate on the case of the higher contrast parameter of $r = 3.5$, where other features observed only in this case are highlighted.

4.1 The structure with weak transverse ligaments

Here $r = 0.5$ and this represents the situation when transverse links in the structure have a lower flexural rigidity to those along the central axis (see Figure 1).

We begin with the highest frequency considered in our simulations, $\omega = 6.25$, in section 4.1.1. This frequency is located near the edge of the pass band $\omega = \sqrt{48}$ for the structure behind the transition front (see Figure 4(a)). With reference to section 3, we describe in detail how to use the theoretical predictions of the model in [26] to accurately analyse and predict all features of the steady-state regimes in the numerical model. It will be shown how these regimes are realised during the transient period of the failure process. Following section 4.1.1, a summary of such predictions and comparison with the numerical results will be provided.

For $\omega = 6.25$ we show there exists one steady state regime representing the case when an evanescent wave is transmitted to the intact structure. Simulations for this frequency ran faster than those for the lower frequencies considered below. As a result of the high load frequency, it is noted that a higher computational accuracy is required to fully capture the behaviour of the structure.

A fairly low frequency of $\omega = 0.6$ is then considered in section 4.1.2. Here, one does not require a comparable computational accuracy as that with the case $\omega = 6.25$. There is need to compute for longer time intervals as convergence to the steady-state transition regime is slow. In addition, we show that more than one steady state regime can be obtained for this frequency. All modes of transition wave propagation studied there are accompanied by waves propagating ahead of the transition point. Interesting features showing how the transient behaviour of the failure wave converges to the steady-state regimes are also reported.

To complete our investigation of the case $r = 0.5$, we end with an intermediate frequency of $\omega = 3$ inside the pass band of the structure when $\eta < 0$. Here, we encounter several regimes of steady-state transition wave propagation and the modes of propagation can be mixed. There, a standard computational accuracy in MATLAB can be used to capture all effects accurately.

4.1.1 Comparison with the steady regime at a higher frequency

For $\omega = 6.25$, only one steady-state speed is observed in the simulations. As predicted by the theory, this speed occurs for the load amplitude interval $91.82 \leq \mathcal{P} \leq 300.8$ and outside this interval the front may propagate non-steadily slower or faster than this speed. Using the method outlined in section 3.5, the analytical solution enables one to determine the load amplitude interval for this regime as $91.37 \leq \mathcal{P} \leq 300.8$, providing a good match with the numerical computations. The difference between both analytical and numerical computations for this interval is attributed to the reason outlined in section 3.2. In Figure 8, we present the results for the average front velocity $\bar{v}$ as a function of $\mathcal{P}$ recorded from the simulations. It is noted that inside the considered interval a plateau is observed, at the value of $v = 2.331$. This speed also corresponds with the speed predicted by the dispersion diagrams (see section 3.4). Indeed, the intersection point of the line corresponding to $\omega = 6.25$ and the curve for $\omega_2(k)$ is $(k, \omega) = (2.6811, 6.25)$. Therefore, the predicted speed for the transition process is given as $v = \omega/k$=2.331. Lower speeds, $v = 0.4099$ and 0.6972, predicted from the dispersion relations are shown on Figure 8, but we note they are never encountered in the simulations. The steady-state regime observed corresponds to the case when no waves transmit ahead of the point $\eta = 0$.

Example profiles of the front position against time are shown in Figure 9(a), for the values

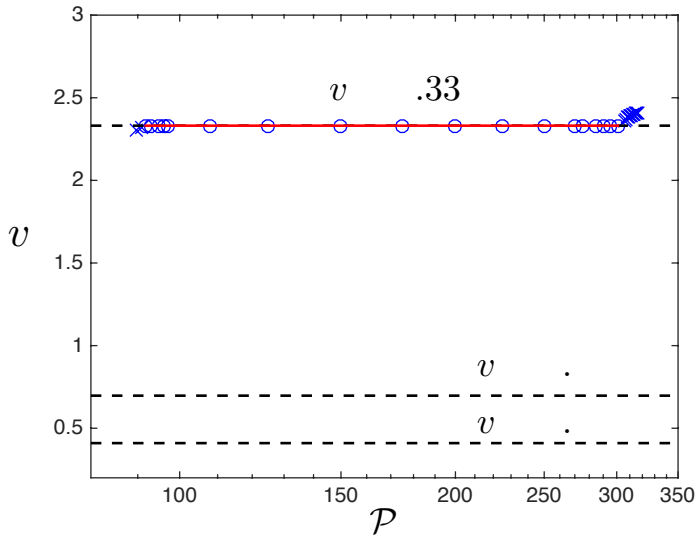

Figure 8: The average transition front speed shown as a function of the quantity $\mathcal{P} = Pa/w_c$, for $\omega = 6.25$ and $r = 0.5$. Here results corresponding to circles represent those for the non-transmission steady-state regime of the transition wave. Crosses indicate the non-steady propagation of the front, where it is noted that the associated average transition wave speed is not equal to predicted steady-state propagation speed of $v = 2.331$.

$\mathcal{P} = 91.82, 158.31$ and 284.96 within the steady-state plateau of Figure 8. Linear profiles can clearly be seen. The average velocity as a function of the transition front position for these values of $\mathcal{P}$ are presented in Figure 9(b). These computations are based on formula (22) in section 3.2. Here we see for all 3 cases we obtain that the average velocity converges to the steady-state speed of $v = 2.331$. The average velocity for $\mathcal{P} = 158.31$, located inside the plateau, converges to this steady-state speed the fastest.

Instantaneous speeds, based on (21) of section 3.2, for the 3 load amplitudes are given in Figure 9(c). For the lowest normalised force amplitude $\mathcal{P} = 91.82$, the distribution of instantaneous speeds appears to be more wider and irregular than for $\mathcal{P} = 158.31$ and 284.96. All 3 amplitudes show that the instantaneous speeds in the transient regime can be very irregular, but as the transition wave propagates inside the structure, they begin to exhibit some regularity as these speeds approach the value $v = 2.331$.

4.1.2 Comparison with the steady regime at a lower frequency

For $\omega = 0.6$, we observe only two transmission modes. The smallest steady-state speed observed is $v = 0.085$ for $\mathcal{P} = 10.06$. Here $v = 0.085$ is also a predicted possible steady-state speed from the dispersion diagrams. For $\mathcal{P}$ increasing past this value, the average transition front speed climbs to the highest possible steady-state speed of $v = 0.7745$ at $\mathcal{P} = 14.63$. Inside $14.63 \leq \mathcal{P} \leq 459$, the average speed is independent of $\mathcal{P}$ and stays at the value $v = 0.7745$. Theoretically, we establish the interval for this steady-state regime as $13.34 \leq \mathcal{P} \leq 460.86$ which produces the theoretical speed $v = 0.7745$. The analytical results provide another good match with the numerical computations. Some lower steady-

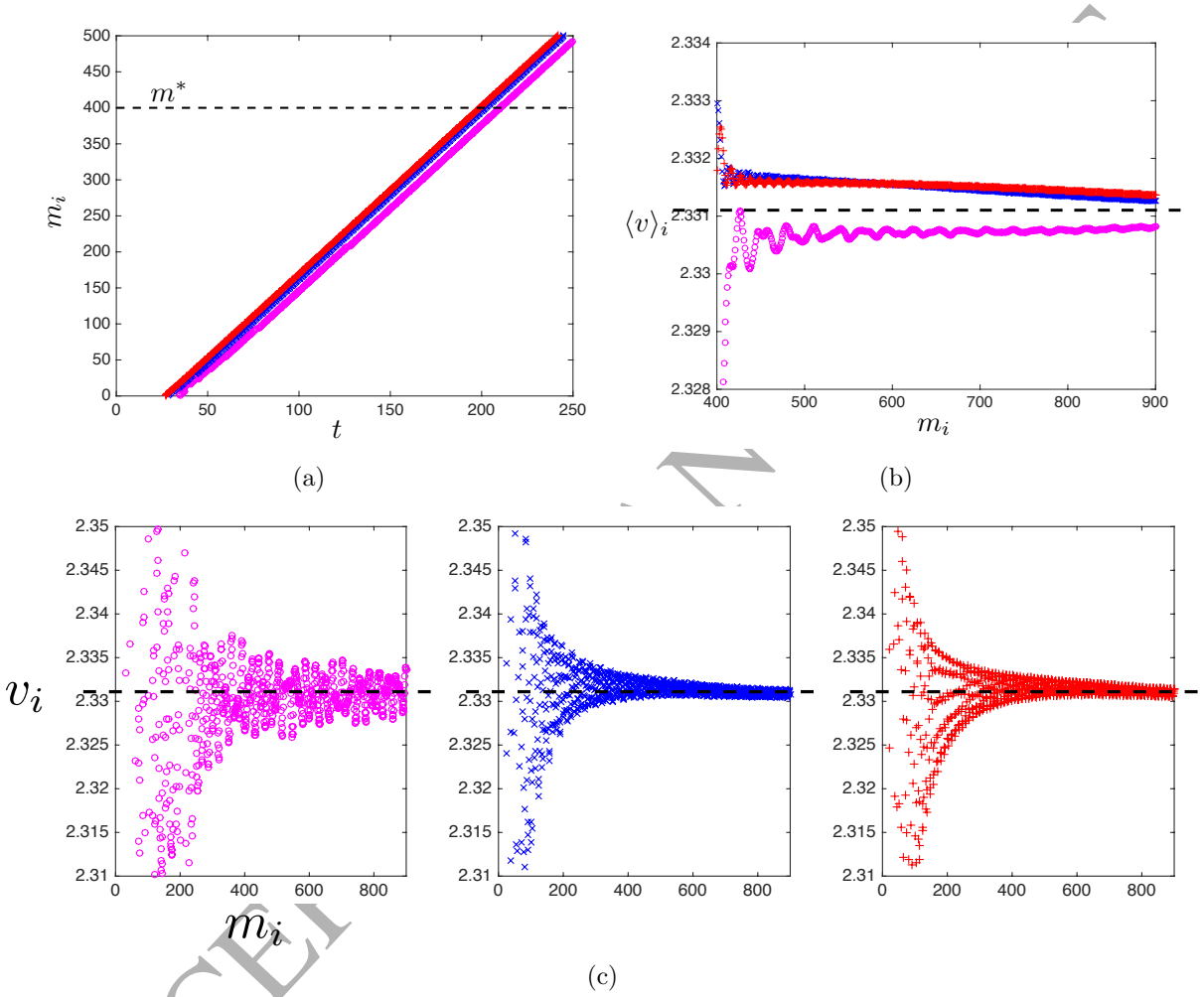

Figure 9: Computations for $\omega = 6.25$, $r = 0.5$. (a) Profiles for transition front position m_i against time t. (b) Average velocities computed using (22) with $m_* = 400$ (shown also in (a)) and (c) instantaneous speeds evaluated using (21) as functions of m_i. Computations are produced for $\mathcal{P} = 91.82$ (pink markers), 158.31 (blue) and 284.96 (red).

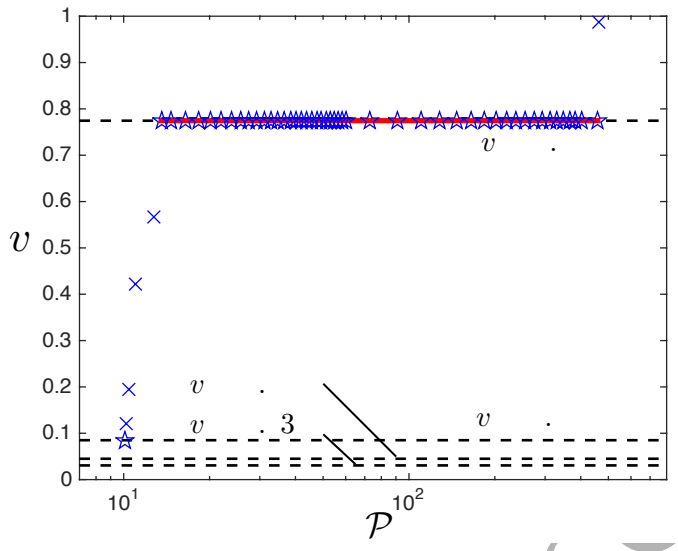

Figure 10: The average transition front speed shown as a function of the quantity $\mathcal{P}$, for $\omega = 0.6$ and $r = 0.5$. In this figure, the stars correspond to the steady-state regime where waves are transmitted ahead of the transition point. Crosses represent regimes with non-steady propagation of the transition wave.

state speeds predicted by the dispersion diagram for $v = 0.0306$ and 0.0450 in Figure 10 are shown by horizontal dashed lines. The front never realises these speeds in the simulations.

In Figure 11(a), we show the transition front position against time for $\mathcal{P} = 18.29, 274.32$ and 457.21 (inside the interval for the highest steady-state regime). These reveal interesting features in the behaviour of the front prior to settling into the steady-state speed. For $\mathcal{P} = 18.29$ the profile is linear from near the start of the transition process. In the cases of $\mathcal{P} = 274.32, 457.21$ one can observe that the front displays a non-uniform speed before reaching the steady-state after approximately 200 and 300 breakages, respectively. It is clear the profile for $\mathcal{P} = 457.21$ displays an overlapping step-like trajectory between the 200th and 300th breakage. This phenomenon is called forerunning fracture, which was first observed in [39] for the separation of a beam from an elastic foundation.

Figure 11(b) shows how the average velocity defined by (22) converges to the steady-state speed in an oscillatory manner. Here it appears the average velocities computed for the cases $\mathcal{P} = 274.32$ and 457.21 converge slower to the steady-state speed than $\mathcal{P} = 18.29$. Clearly the convergence to $v = 0.7745$ here worsens with increase of $\mathcal{P}$, which is a result of the time taken to reach this steady-state regime.

In Figure 11(c), the average velocities computed using $m_*(t^*) = 1$ (i.e. from the start of the transition process) are shown. The results illustrate that for $\mathcal{P} = 18.29$ we converge to the speed $v = 0.7745$ the fastest. Computations for $\mathcal{P} = 274.32$ and 457.21 show they approach the steady-state speed slower than those for $\mathcal{P} = 18.29$, as in this case non-steady propagation of the transition front is observed at the start of the simulation (see Figure 11(a)). Figures 11(b) and 11(c) illustrate the sensitivity of (22) to the choice of p^* and t^*.

The instantaneous speed distribution as a function of fracture position is given in Figure 11(d). There, it is observed that the convergence to the transition front speed $v = 0.7745$

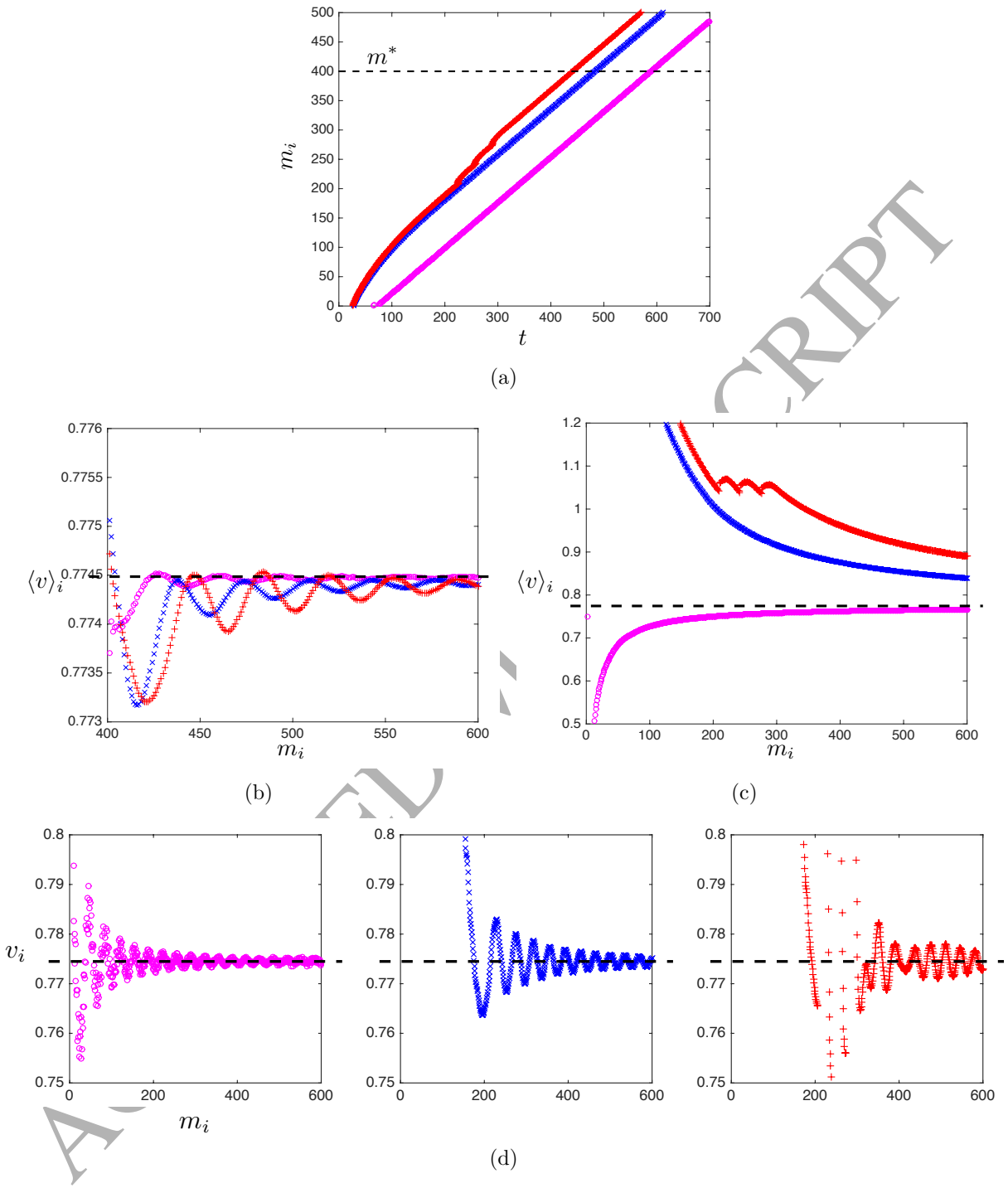

Figure 11: For $\mathcal{P} = 18.29$ (pink markers), 274.32 (blue) and 457.21 (red), in (a) we show the transition wave position m_i as a function of time t. As functions of m_i, we present (b) the average velocity $\langle v\rangle_i$ computed with (22) from the 400th breakage ($m_* = 400$, see in (a)), and (c) from the 1st breakage ($m_* = 1$). The instantaneous velocities v_i for the transition front are given in (d). Computations are based on the parameters $\omega = 0.6$, $r = 0.5$.

becomes slower with increase of $\mathcal{P}$. The instantaneous speeds in fact oscillate about $v = 0.7745$. For $\mathcal{P} = 18.29$, the instantaneous speeds begin to oscillate about this speed from the first breakage. Increasing $\mathcal{P}$ shows these oscillations about $v = 0.7745$ begin much later in the simulations. It is also interesting to note the size of oscillations towards the end of each simulation decreases as we decrease $\mathcal{P}$.

4.1.3 Comparison with the steady regime at an intermediate frequency

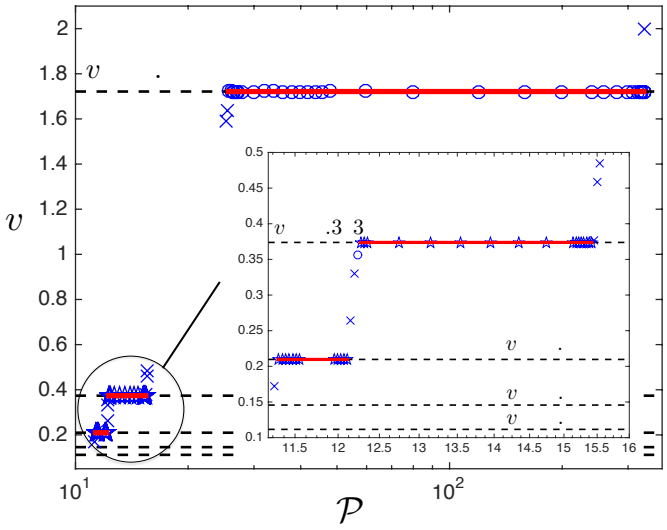

Figure 12: The average transition front speed shown and its dependence on the quantity $\mathcal{P}$, for $\omega = 3$, $r = 0.5$. Here results corresponding to (i) circles represent those for the non-transmission steady-state regime, (ii) stars are those for the steady-state transmission regime and (iii) crosses indicate the non-steady transition wave propagation when the system has settled.

Here, the theoretical predictions show that the fourth largest steady-state speed is impossible as the prediction for minimum value of $\mathcal{P}$ to observe such a regime is greater than the predicted value representing the end of this regime. In addition, any speed lower than this speed is not observed here.

For $\omega = 3$, as predicted by the theory only 3 different speeds $v = 0.2097, 0.3837, 1.7214$ are observed in the simulations, inside the intervals $11.31 \leq \mathcal{P} \leq 12.11$, $12.27 \leq \mathcal{P} \leq 15.42$ and $25.62 \leq \mathcal{P} \leq 330.72$, respectively, shown in Figure 12. These speeds are shown as plateaus in this Figure, depicting the average transition wave speed $\bar{v}$ as a function of $\mathcal{P}$. We note that there are no steady-state speeds lower than 0.2097 observed in this case, but some representative speeds for $v = 0.1116$ and $v = 0.1457$ are indicated by the horizontal dashed rays in the inset of Figure 12. The speeds $v = 0.2097$ and $v = 0.3837$ correspond to modes of transition front propagation where waves are transmitted ahead of this point. The speed $v = 1.7214$ corresponds to the propagation regime where an evanescent wave is transmitted ahead of the front.

For the highest steady-state speed of $v = 1.7214$ the value $\mathcal{P} = 25.62$, represents the first time the transition front is observed to propagate steadily with speed 1.7214. In addition, the value $\mathcal{P} = 25.62$ is the theoretical prediction for the minimum value of $\mathcal{P}$ required to propagate the transition front at the highest steady-state speed $v = 1.7214$. Therefore, we have an excellent agreement between the result of the simulations and theory. Further, $\mathcal{P} = 330.72$ represents the end of the highest steady-state regime (discussed in section 3.5), which is again predicted by the analytical solution for w_+ in (15). Thus, the theory presented in section 2 shows the numerical model for the transient problem is correct for these parameters.

The intervals presented for $\mathcal{P}$ here are discrete and monotonically increase in size (as in the case $\omega = 0.6$). Outside these intervals, the average transition can propagate non-steadily. The corresponding average transition front speeds are not equal to any of the predicted steady-state speeds. In particular, for $\mathcal{P} = 330.77$, Figure 12 shows the front can propagate faster than the highest steady-state speed. The non-steady propagation mode, which corresponds to a more complicated but organised regime, will not be discussed in detail here.

Further, we investigate the normalised instantaneous speeds for $\omega = 3$ (normalised by the average fracture speed, observed during the steady-state fracture processes). In Figure 13(a), we show the normalised instantaneous speed distribution corresponding to values of $\mathcal{P}$ located inside the plateaus that produce the speeds $v = 0.2097$, 0.3738 and 1.7214 ($\mathcal{P} = 11.53, 12.35$ and 39.84, respectively). It is clear that as $\mathcal{P}$ increases, the instantaneous speed distribution takes longer to settle to the steady-state speed. For example, $\mathcal{P} = 39.84$ shows a wider instantaneous speed distribution in the breakage of the first 170 links.

Next for $\mathcal{P} = 26.29$, 159.36 and 318.72, we investigate the transition process as a function of time and the corresponding instantaneous and average speed distributions. These values of $\mathcal{P}$ are located at the beginning, middle and end of the plateau identified for the highest steady-state regime $v = 1.7214$ in Figure 12.

The position of the transition front as a function of time is shown in Figure 13(b). For $\mathcal{P} = 318.72$ the steady-state regime is obtained after a much longer time interval than those for $\mathcal{P} = 26.29$ and 159.36. In fact, it is not until after approximately the first 170 links that the steady-state regime begins.

Average speeds, calculated using (22), are shown in Figure 13(c) as a function of the transition wave position. Data up to the 900^{th} breakage are presented. From left to right, we show the average speed distribution recorded from the starting points $m_*(t^*) = 200$, 300 and 400, respectively. Horizontal dashed lines of where these starting points correspond to are shown for the fracture profiles of Figure 13(b). The average speed distribution in all 3 figures is shown to approach the steady-state speed $v = 1.7214$. Here we show that the average speed defined by (22) is sensitive to the choice of m_*. As m_* is increased, we see a faster convergence of the average speed distribution to $v = 1.7214$. In addition, the results for $\mathcal{P} = 159.36$ are shown to converge to this speed faster than those for $\mathcal{P} = 26.29$ and $\mathcal{P} = 318.72$ for all 3 values of m_*.

In Figure 13(d), the instantaneous speeds as a function of the fracture position are given from left to right, for $\mathcal{P} = 26.29$, 159.36 and 318.72, respectively. We present the data for 900 breakages. In all 3 figures, the instantaneous speed distribution is wider near the start of the simulations. Eventually, it can be seen that the width of the distribution narrows

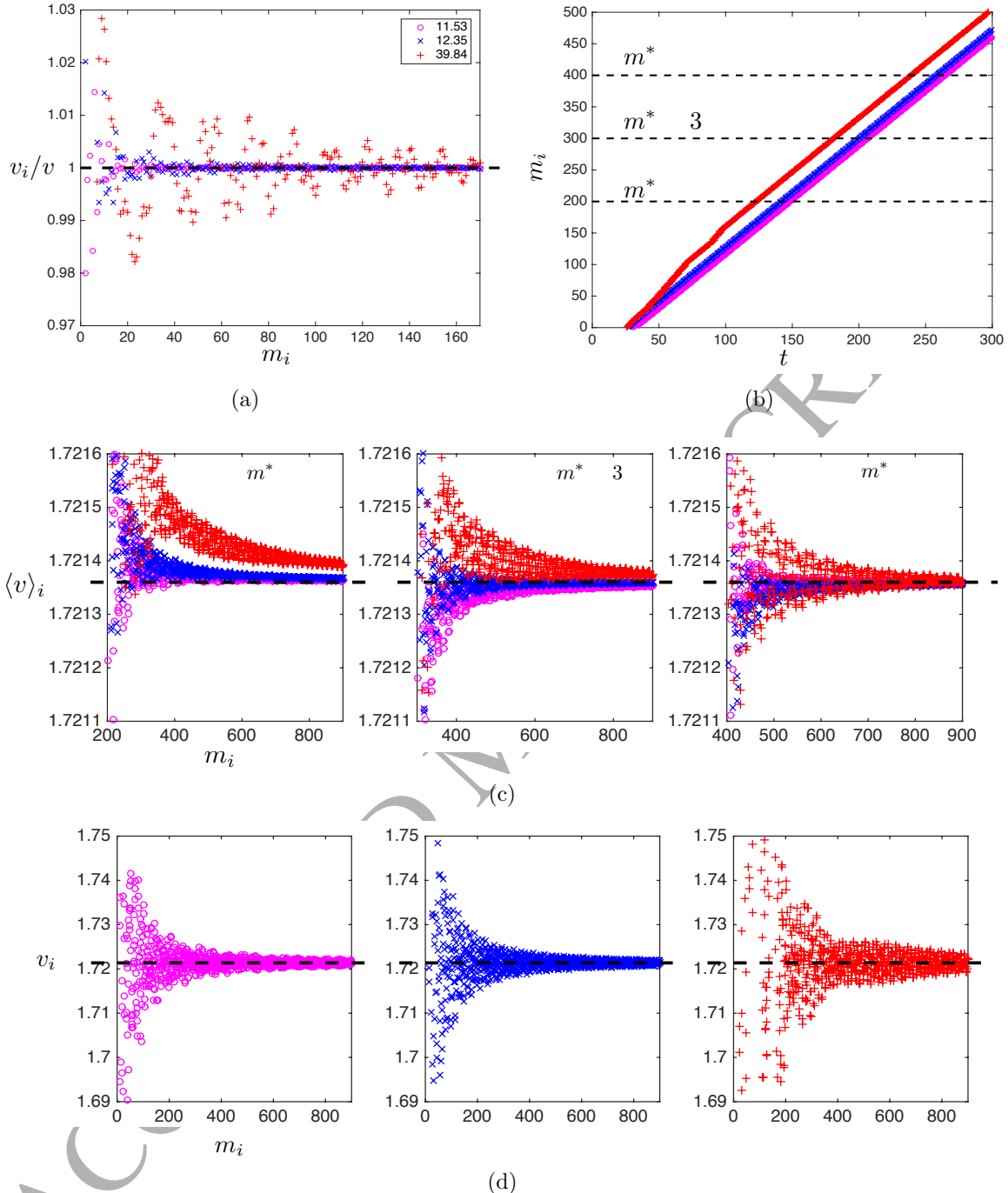

Figure 13: Computations for the case $\omega = 3$ and $r = 0.5$. (a) Instantaneous speeds computed using (21) for the speeds $v = 0.2097$ (pink circles), 0.3837 (red crosses) and 1.7214 (blue crosses). There the results are normalised by the corresponding observed steady-state propagation velocity. (b) The position of transition front m_i as a function of time t. (c) The average velocities $\langle v\rangle_i$ (computed using (22)) as a function m_i, for various values of $m_* = 200, 300, 400$ (indicated in (b)). (d) The instantaneous speeds v_i and their dependency on m_i. For (b)–(d), results have been produced for $\mathcal{P} = 26.29$ (pink markers), 159.36 (blue) and 318.72 (red).

as the simulation continues to run. There the instantaneous speeds appear to converge to $v = 1.7214$. For $\mathcal{P} = 159.36$, the distribution of instantaneous speeds appear more regular and converge to the speed $v = 1.7214$ quicker than those for $\mathcal{P} = 26.29$ and $\mathcal{P} = 318.72$.

Profile ahead of the transition front. First, for $\mathcal{P} = 39.84$, we present in Figure 14(a), computations resulting from the numerical model for the transient problem compared with the numerical computations of the inverse Fourier transform of the solution to the Wiener-Hopf equation, as discussed in section 3.5. Another good agreement between the mass displacements extracted from the simulations and the theoretical results of [26] is demonstrated. In accordance with the case $\mathcal{P} = 330.72$ discussed in section 3.5, for $\mathcal{P} = 39.84$ the central beam of the structure ($y = 0$) exhibits a maximum located inside $\eta > 0$. This occurs approximately at the point $\eta = 3$ and here $w/w_c = 0.15$. We confirm with this Figure 14(a), that there is only an evanescent wave transmitted into the intact structure.

Inclination behind the transition front. Here, we comment on the behaviour of the beam strip behind the transition front as a function of the load amplitude. In Figure 14(b), we show various profiles of the structure produced from the computations in MATLAB for $\omega = 3$ and different values of the ratio $\mathcal{P}$. For these parameters, after reaching the steady-state regime, the transition wave propagates steadily with the speed of 1.7214 and an evanescent mode is transmitted into the region $\eta > 0$. The case when a wave propagates ahead of the transition point and the inclination is observed during the steady-state regime was discussed earlier in section 3.6.

Figures 14(b)–14(d) demonstrate that when $\mathcal{P}$ is increased, the slope of the beam structure, defined relative to the front at $\eta = 0$ also decreases. In addition to the MATLAB data provided in Figure 14(c), we provide the plot of the analytical prediction A_s for the inclination as a function of $\mathcal{P}$ based on (27). The result is shown as a solid black line. In Figure 14(d), we also present a comparison of the MATLAB results with the those given by (27) for a larger range of $\mathcal{P}$ to understand how the slope behaves as a function of $\mathcal{P}$. The slope A_s exhibits a linear behaviour as "$\mathcal{P} \to \infty$".

Once again, in Figures 14(c) and 14(d), we see an excellent agreement between the numerical experiments in MATLAB and the theoretical prediction for A_s. It is worth mentioning that as the ratio $\mathcal{P} \to \Lambda$ (see (25)), the slope $A_s \to 0$. As discussed in [26], this limit physically implies the the kinetic energy of the masses along the inclination is zero.

4.2 The structure with stiff transverse ligaments

We now numerically study the transient problem of failure wave propagation inside a finite structure with a higher heterogeneity, $r = 3.5$. In this case, we show that one can encounter a mixture of features observed for the various frequencies considered when $r = 0.5$. We begin again with $\omega = 6.25$ in section 4.2.1 and demonstrate that more steady-state regimes are observed for this frequency than in the case of $r = 0.5$. In addition, we consider a lower frequency of $\omega = 1.5$ in section 4.2.2 and reveal some surprising phenomena concerning the transition wave speed, which us associated with the minimal feeding wave energy required for its steady propagation.

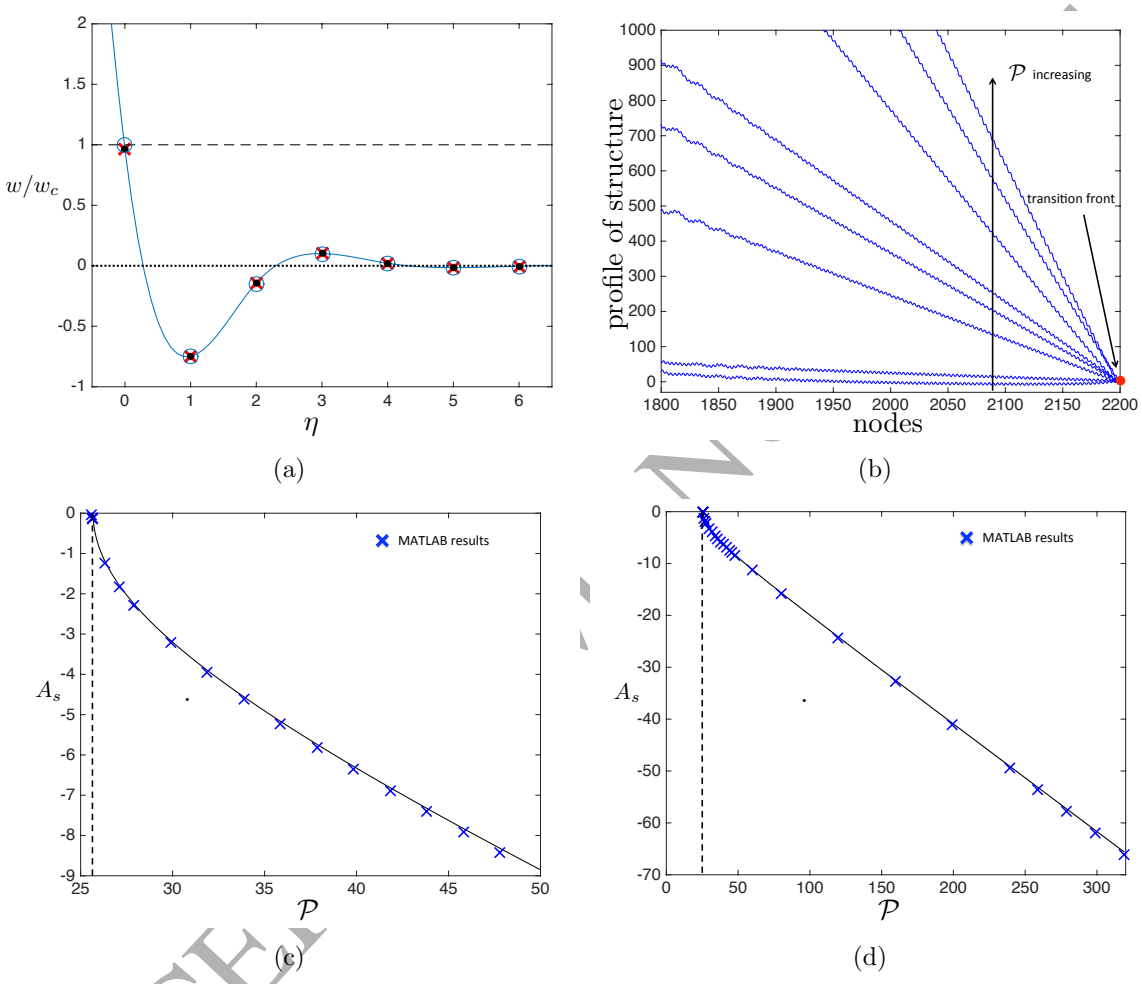

Figure 14: (a) Profiles ahead of the transition front as a function of η for $\omega = 3$, $r = 0.5$ and $\mathcal{P} = 39.84$. (b) The profile of the structure as a function of the node number m, for $\mathcal{P} = 25.61, 25.62, 26.29, 27.09, 27.89, 31.87, 35.86$ and 39.84. (c) & (d) The plot of (27) as a function of $\mathcal{P}$ (solid line) and corresponding MATLAB results (crosses). Also shown in both (c) and (d) is the value $\Lambda = 25.62$, where $A_s = 0$.

4.2.1 Comparison with the steady regime at a higher frequency for the stiffer structure

We once again observe more than one steady-state speed of the transition front. As the theory predicts, the steady-state speeds $v = 0.4099$, $v = 0.6972$ and $v = 2.331$ occur for $94.2 \leq \mathcal{P} \leq 100.3$, $105.1 \leq \mathcal{P} \leq 107.1$ and $416.6 \leq \mathcal{P} \leq 5951$, respectively. We note that the number of such states is completely different from that encountered for the same frequency for $r = 0.5$.

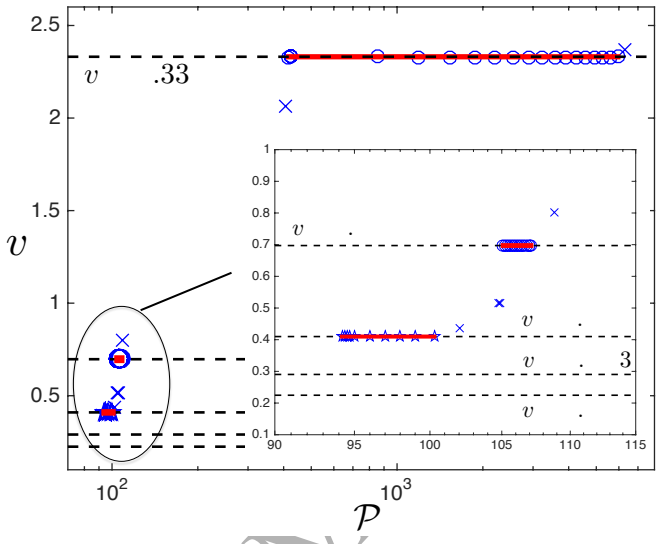

Figure 15: The average transition front speed as a function of the quantity $\mathcal{P}$, for $\omega = 6.25$ and $r = 3.5$. See Figure 12 for the description of the markers.

Moreover, in comparison with the case $\omega = 3$ and $r = 0.5$, the size of the intervals for $\mathcal{P}$ corresponding to steady-state speeds is not monotonic with respect to the front speed. A transmission regime is observed for the speed $v = 0.4099$, whereas for the speeds $v = 0.6972$ and 2.331 only an evanescent wave propagates ahead of the transition front. This shows that the modes corresponding to the transition front propagation may alternate with increase of the transition wave steady-state speed, which was not observed for $\omega = 3$, $r = 0.5$. Lower speeds $v = 0.2247$ and 0.2903 predicted by the dispersion relations are also shown in Figure 15 by horizontal dashed rays and it is noted we do not observe propagation of the front at these speeds.

For the highest steady-state regime, the profiles for $\mathcal{P} = 425.1, 578.13$ and 5951.37 are shown in Figure 16(a). Here the linear profiles can be seen, which correspond to the speed $v = 2.331$. In addition, if one analyses the average velocity of the transition wave using (22), it is noticed that the results for $\mathcal{P} = 578.13$ converge faster to the predicted steady-state speed. The value of $\mathcal{P} = 578.13$ is located inside the steady-state plateau for $v = 2.331$ in Figure 15. The instantaneous speeds are presented in Figure 16(c). We see that initially, the transition front can propagate with an irregular distribution of instantaneous speeds. For example, we refer to the case $\mathcal{P} = 425.1$ in Figure 16(c), which corresponds to the start of the plateau for $v = 2.331$ on Figure 15. The transient behaviour of the failure process

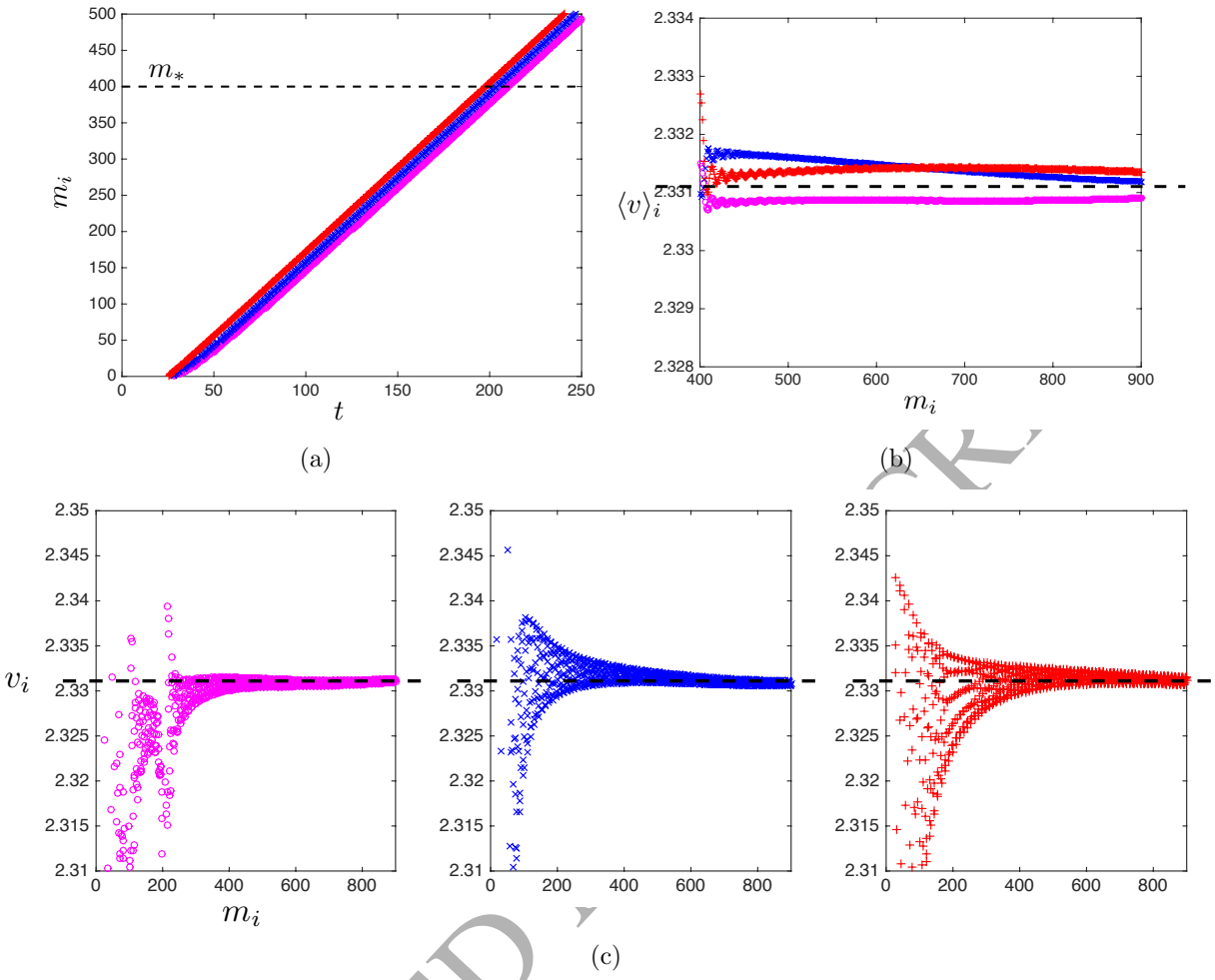

Figure 16: Here we show for $\omega = 6.25$, $r = 3.5$ (a) transition front position m_i and its dependency on time t, (b) average velocities $\langle v \rangle_i$ of the front (using (22), with $m_* = 400$, as depicted in (a)) and (c) instantaneous speed distributions v_i as function of m_i, for $\mathcal{P} = 425.1$ (pink markers), 578.13 (blue) and 5951.37 (red).

appears to more regular with increase in $\mathcal{P}$. For all values presented in Figure 16(c), the instantaneous speeds converge to the predicted steady-state behaviour $v = 2.331$.

4.2.2 Comparison with the steady regime at a lower frequency on the stiffer structure

Finally, consider a lower frequency of $\omega = 1.5$. Here we identify only one steady-state speed $v = 1.223$, as expected, which corresponds to the highest predicted steady-state speed of the front. This regime also represents a transmission mode and it occurs for $117.5 \leq \mathcal{P} \leq 1037$ (indicated by the plateau in Figure 17, which shows the average transition wave speed $\bar{v}$ as a function of $\mathcal{P}$).

Inside the steady-state plateau for $v = 1.223$, we consider the values $\mathcal{P} = 110.61$, 532.32 and 1036.99. The position of the transition front as a function of time during the correspond-

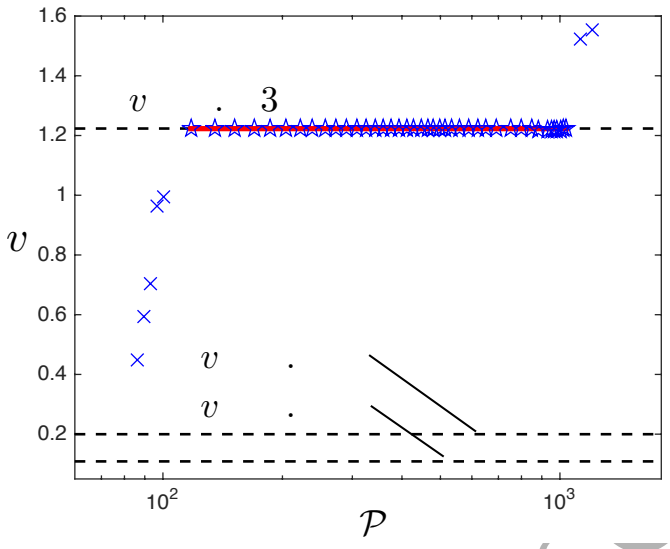

Figure 17: The average transition front speed shown as a function of the quantity $\mathcal{P}$, for $\omega = 1.5$ and $r = 3.5$. The description of markers can be found in Figure 12.

ing regimes are shown in Figure 18(a). Here the results for $\mathcal{P} = 110.61$ and 532.32 show linear profiles, but for $\mathcal{P} = 1036.99$, we observe that initially the front speed is non-uniform up to the approximately the 160th breakage.

Average velocities computed using (22), as a function of the transition front position, are shown in Figure 18(b). Here, the average velocities for $\mathcal{P} = 532.32$ and 1036.99 display an oscillating behaviour and converge quickly to the predicted speed of 1.223. In addition, the convergence to this speed occurs the fastest for $\mathcal{P} = 532.32$. It is interesting to note that the behaviour in the average velocities for $\mathcal{P} = 110.61$ is unexpected, as they do not exhibit a similar trend to those for $\mathcal{P} = 532.32$ and 1036.99. In fact, the average velocities form two distinct bands that appear to approach the line for $v = 1.223$ from above and below.

In particular, one can identify more interesting features for the case $\mathcal{P} = 110.61$ by observing the associated instantaneous speeds. In Figure 18(c), we show the instantaneous speeds computed with (21) as a function of the transition wave position. For $\mathcal{P} = 532.32$ and 1036.99 the instantaneous speeds distribute close to and around the speed $v = 1.223$. This happens in such a way that the width of the distribution narrows as the front propagates further through the structure and the instantaneous speeds approach the line for $v = 1.223$. In contrast, when $\mathcal{P} = 110.61$, we see a completely different instantaneous speed distribution. In the first 400 breakages, the instantaneous speeds in this case appear to be distributed randomly about the line $v = 1.223$. Beyond the 400th breakage, we can identify the emergence of 5 distinct bands for the instantaneous speeds, above and below the line $v = 1.223$. Interestingly, the average of these instantaneous speeds gives the average front speed as 1.223.

To understand how a distribution of instantaneous speeds develops from, for example, that for $\mathcal{P} = 110.61$ to those typical for $\mathcal{P} = 532.32$ and 1036.99, we show in Figures 19(a) and 19(b) the evolution of the distribution as we increase $\mathcal{P}$. In these figures, we see that the instantaneous speed distribution in the first 300 breakages appears to be randomly

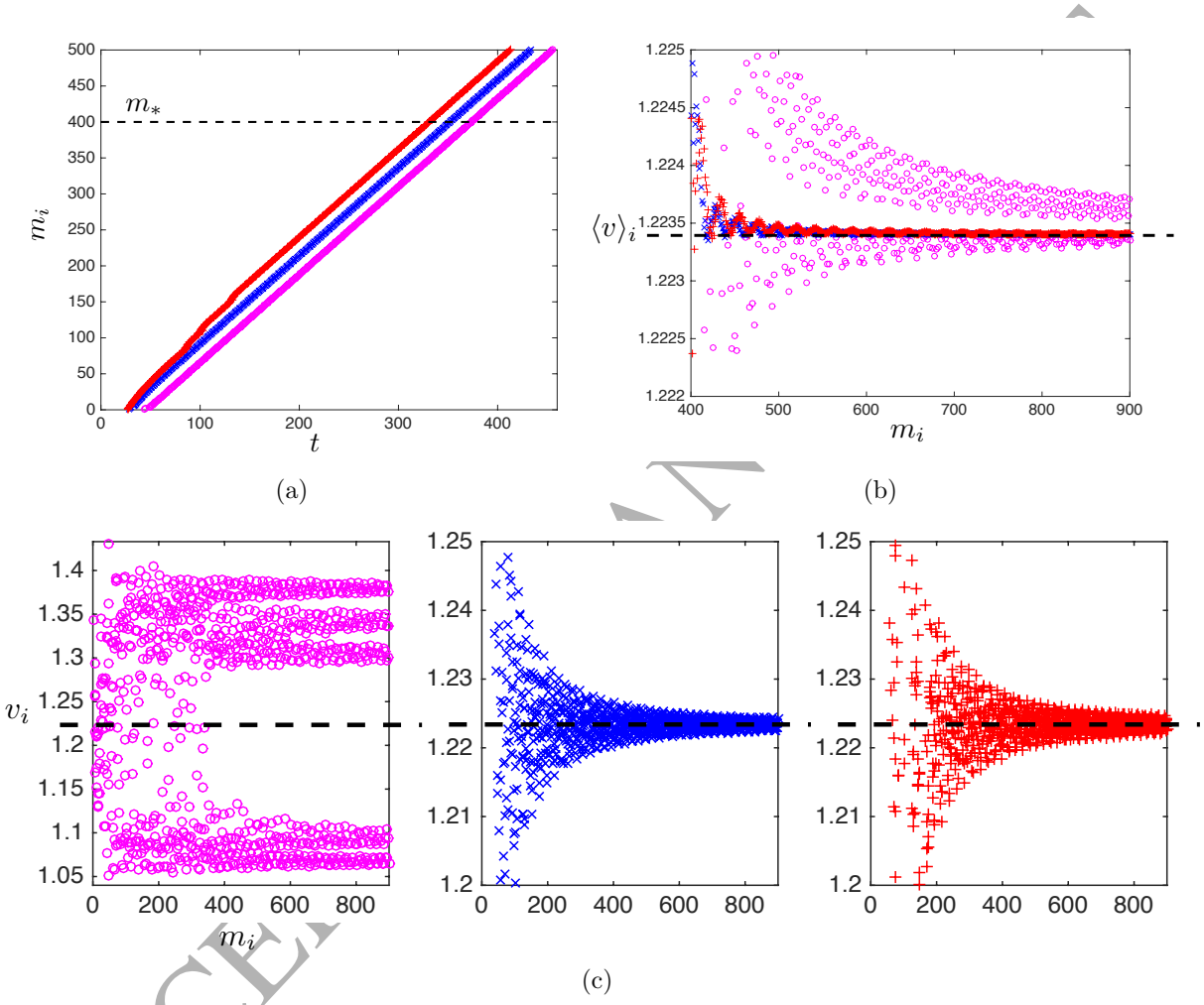

Figure 18: (a) The transition wave position m_i as a function of time t. (b) The average velocities v_i as a function of m_i, based on (22) with $m_* = 400$. (c) Instantaneous speed distributions v_i and its dependency on m_i. Computations are performed for $\mathcal{P} = 110.61$ (pink markers), 523.32 (blue) and 1036.99 (red), with $\omega = 1.5$, $r = 3.5$.

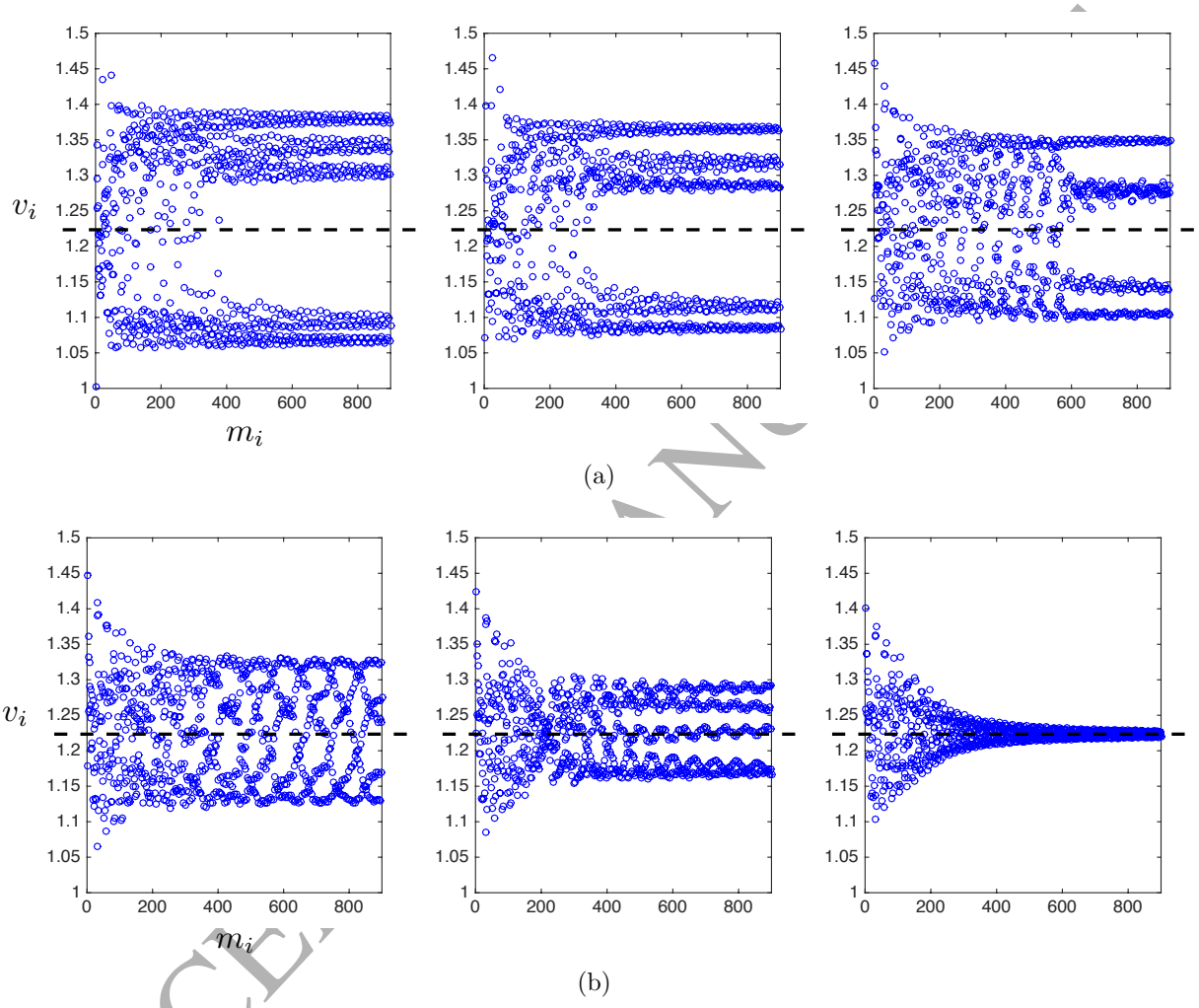

Figure 19: The instantaneous velocities v_i for $\omega = 1.5$, $r = 3.5$ and $v = 1.223$, based on (21), as a function of the transition wave position m_i. We present the computations in (a) for $\mathcal{P} = 110.61, 114.07$, 117.53, (from left to right) and (b) 120.98, 124.44 and 127.89 (from left to right).

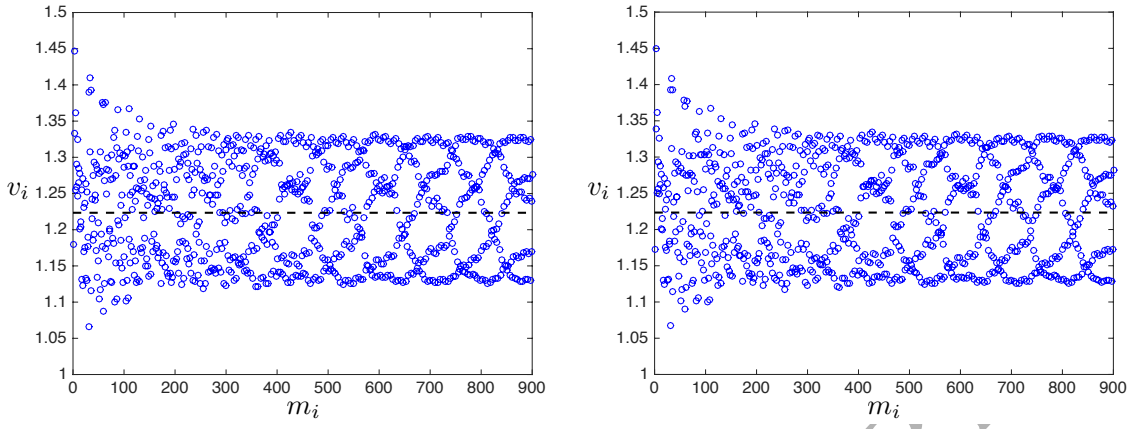

(a) (b)

Figure 20: Instantaneous velocities v_i, produced according to (21), as a function of the transition wave position m_i, for $\mathcal{P} = 120.98$. While the instantaneous velocities appear to be randomly distributed inside a band of finite width within the fist 300 breakages, beyond this point they arrange themselves in the formation of a woven mesh. In (a) we show the computations performed with a relative tolerance of 10^{-3}, whereas in (b) the computations are produced using a relative tolerance of 10^{-5} in MATLAB. The results are very similar.

distributed within a regular envelope. In what follows, we focus on the instantaneous speed distribution beyond the 300th breakage. We begin in Figure 19(a), from the left where $\mathcal{P} = 110.61$ (discussed above) and gradually increase $\mathcal{P}$. In going to $\mathcal{P} = 114.07$ it is observed that the multiple bands of instantaneous speeds shown for $\mathcal{P} = 110.61$ become narrower. The number of these bands reduce from 5 to 4, for $\mathcal{P} = 117.53$ and we also see an regular arrangement of instantaneous speeds between the 200th and 600th breakage. When $\mathcal{P} = 120.98$, a regular woven mesh pattern appears as part of the instantaneous speed distribution. Comparing the cases $\mathcal{P} = 110.61$ through to 120.98, we see the width of the instantaneous speed distribution narrows around $v = 1.223$. Increasing to $\mathcal{P} = 124.44$, 4 distinct lines for the instantaneous speeds can be observed, within an interval that continues to narrow. Finally, when $\mathcal{P} = 127.89$ the typical instantaneous speed distribution observed in Figure 18(c), for $\mathcal{P} = 532.32$ and 1036.99, is achieved.

In Figure 20, we show the instantaneous speed distributions for $\mathcal{P} = 120.98$ obtained from the MATLAB computations with different relative tolerances. In Figure 20(a), the relative tolerance used in MATLAB to produce these computations was 10^{-3}, whereas in Figure 20(b) the relative tolerance used was 10^{-5}. We note that both sets of results are visibly the same and the maximum error between the results near the end of the computational window is of the order 10^{-3} .

5 Discussion and conclusions

We have presented the analysis of a transient problem for a transition wave propagating inside a heterogeneous finite structure composed of beams and periodically placed masses

that is subjected to a remote point load. The results in [26] concerning the same process in an infinite beam structure have been given and used to provide predictions of what happens for the finite structure. Excellent agreement between the numerical results and the theoretical predictions were obtained for the steady-state regimes, confirming the numerical approach to the transient problem is correct and simultaneously proving that the theoretical predictions can be trusted.

For various load frequencies and different choices of the heterogeneity parameter, we analysed the average speed of the fracture front as a function of the load amplitude. We identified intervals for the load amplitude where steady-state fracture speeds were encountered. Note that the interval size is not always a monotonic function of the fracture speed. Outside these intervals, the front propagates non-steadily. The realised steady-state speeds corresponded with those predicted by the dispersion relations for the structure. The load amplitude intervals also were shown to agree very well with those predicted by the theoretical model.

We note that for different cases of loading and heterogeneity parameters, the number of steady-state speeds encountered varied both with change in load frequency and the structural heterogeneity. While theoretically, the dispersion diagrams offers an infinite list of predictions for the transition front speeds, not all are realised in practice. In fact, at most at, we encountered 3 possible speeds predicted by the dispersion diagram and this information can be obtained from the theoretical analysis.

Also encountered in the numerical simulations were various dynamic features of the structure during the steady fracture process. For instance, there is always a slope behind the transition front during this process, in addition to waves transmitted and reflected from this interface. Properties of these features can also be traced from the theoretical model of [26].

The numerical model sheds more light on how specific steady-state regimes are realised whereas the theoretical approach of [26] does not. Using both the notion of instantaneous front velocities and the average velocity of the front, we have demonstrated that following the initiation of the transition process in the finite structure, the speed of transition wave converges to the predicted steady-state speeds. In addition, in analysing the instantaneous speed distribution of the transition front, we can observe some behaviour not typical of the steady-state transition process. By this, we refer to the results of section 4.2.2, which show how the transition wave speed can follow a regular pattern exhibiting several possible instantaneous speeds, but none of these speeds take a value equal to the steady-state speed.

In the transient problem that was studied numerically, when the failure wave speed converges to the steady-state propagation regime one can observe regular fluctuations in the instantaneous speed of this wave. We refer to Figure 21, where within the steady-state regime, the instantaneous speeds are seen to arrange themselves in a regular fashion and, in an averaged sense, they produce a good agreement with the predicted steady-state speed. We add that this phenomenon is not captured in model of [26], which assumes the uniform propagation of the transition wave.

The investigation presented here shows there exists non-steady regimes of propagation for the fracture process. This brings us to an interesting question: "Is it possible to use the theoretical model of the steady-state transition process to predict non-steady regimes which are regular in a sense?". Such regimes may include clustering and forerunning regimes observed in [21] and [39], respectively. The preliminary answer, based on the results presented

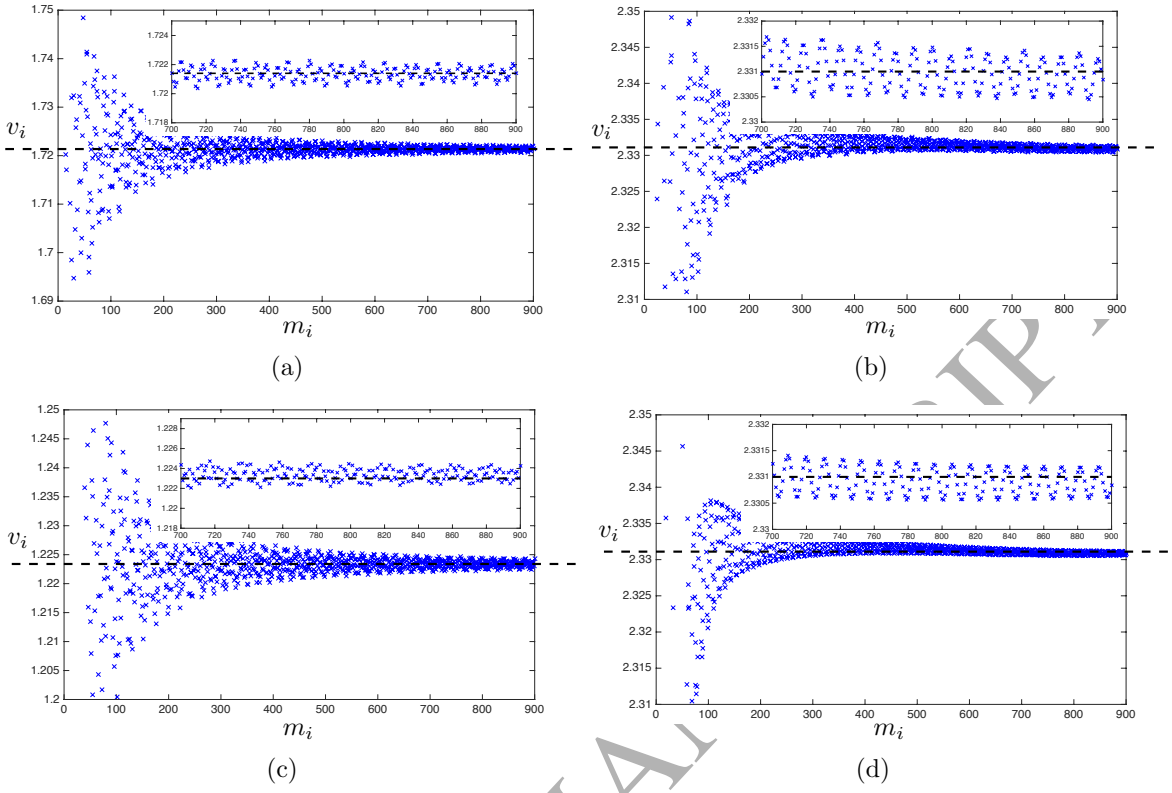

Figure 21: Instantaneous speeds of the transition wave as a function of its position. The diagrams are computed for (a) $\omega = 3$, $r = 0.5$, $\mathcal{P} = 159.36$, (b) $\omega = 6.25$, $r = 0.5$, $\mathcal{P} = 158.31$, (c) $\omega = 1.5$, $r = 3.5$, $\mathcal{P} = 523.32$ and (d) $\omega = 6.25$, $r = 3.5$, $\mathcal{P} = 578.13$. On the inset of these figures we show the instantaneous speed distribution for the last 200 breakages within the structure. It can be seen in each case, the data for v_i is arranged in a regular fashion, that does not necessarily equal the predicted steady-state speed depicted by the horizontal dashed line.

here and [26], shows that this answer is positive.

Acknowledgement: The authors gratefully acknowledge the financial support of the European Seventh Framework Programme under contract no.s PIAP-GA-2012-284544-PARM2.

References

[1] Albuquerque, E. L., Sollero, P., Aliabadi, M. H. (2004) Dual boundary element method for anisotropic dynamic fracture mechanics International Journal for Numerical Methods 59, no. 9, 1187?1205

[2] M. H. Aliabadi (1997): Boundary element formulations in fracture mechanics Appl. Mech. Rev 50, no. 2, 83-96 doi:10.1115/1.3101690

[3] Armero, F., Linder, C.: (2009) Numerical simulation of dynamic fracture using finite elements with embedded discontinuities, International Journal of Fracture 160, 119–141.

[4] Bažant, Z.P., ASCE, F., Verdure, M., (2007): Mechanics of Progressive Collapse: Learning from World Trade Center and Building Demolitions, J. Engn. Mech. 133, 308-319.

[5] Bouchbinder, E., Fineberg, J., Marder, M. (2010): Dynamics of simple cracks, Annu. Rev. Condens. Matter Phys. 1, 371?395.

[6] Brun, M., Giaccu, G.F., Movchan, A.B., Slepyan, L.I. (2014): Transition wave in the collapse of the San Saba Bridge, Front. Mater. http://dx.doi.org/10.3389/fmats.2014.00012.

[7] Brun, M., Movchan, A.B., Slepyan, L.I. (2013): Transition wave in a supported heavy beam, Journal of the Mechanics and Physics of Solids 61, 2067–2085.

[8] Camacho, G.T., Ortiz, M. (1996): Computational modelling of impact damage in brittle materials, Internation Journal of Solids and Structures 33, no. 20–22.

[9] Deegan, R.D., Petersan, P.J., Marder, M., Swinney, H. L. (2002): Oscillating fracture paths in rubber, Physical Review Letters 88, no. 1, doi: 10.1103/PhysRevLett.88.014304.

[10] Deegan, R.D., Chheda, S., Patel, L., Marder, M., Swinney, H.L. (2003): Wavy and rough cracks in silicon, Physical Review E 67, 066209.

[11] Fedelinski, P., Aliabadi, M.H., Rooke, D.P. (1993): The dual boundary element method in dynamic fracture mechanics Engineering Analysis with Boundary Elements 12, no. 3, 203–210.

[12] Gallagher, R.H., A Review of Finite Element Techniques in Fracture Mechanics, Numerical Methods in Fracture Mechanics, Proc. of the 1st Int. Conf., ed. by A. R. Luxmoore and D.R.J. Owens, Univ. College Swansea, p. 1, Jan. 1978.

[13] Gorbushin, N. and Mishuris, G. (2016): Dynamic crack propagation along the interface with non-local interactions, Journal of the European Ceramic Society, doi:10.1016/j.jeurceramsoc.2015.12.048.

[14] Isobe, D. and Tsuda, M., (2003): Seismic collapse analysis of reinforced concrete framed structures using finite element method, Earthquake Engng Struct. Dun., 2027–2046.

[15] Kaewkulchai, G., Williamson, E.B., (2004): Beam element formulation and solution procedure for dynamic progressive collapse analysis, Computers and Structures 82, 639–651.

[16] Kobayashi, A.S.: Numerical Analysis in Fracture Mechanics, Application of Fracture Mechanics to Materials and Structures, Editors: G.C. Sih et al., Martinus Nijhoff Publishers, The Hague 1984.

[17] Kozinov, S., Kuna, M. (2015): Numerical analysis of fracture of pre-stressed ferroelectric actuator taking into account cohesive zone for damage accumulation. 7th ECCOMAS Thematic Conference on Smart Structures and Materials, SMART 2015, Editors: A.L. Araúo, C.A. Mota Soares, et al. (SMART 2015).

[18] Jacobs, J.A. (1950): Relaxation methods applied to problems of plastic flow I, Notched Bar Under Tension, Phil. Mag., 41, p47.

[19] Marder, M. (2004): Effects of atoms on brittle fracture, International Journal of Fracture 130, 517?555.

[20] Marder, M., Gross, S., (1995): Origin of crack tip instabilities. J. Mech. Phys. Solids 43, (1), 1-48.

[21] Mishuris, G.S., Movchan, A.B., Slepyan, L.I. (2008): Dynamical extraction of a single chain from a discrete lattice, Journal of the Mechanics and Physics of Solids 56, 487?495.

[22] Mishuris, G.S., Movchan, A.B., Slepyan, L.I. (2008): Dynamics of a bridged crack in a discrete lattice, Q. Jl Mech. Appl. Math. vol. 61, no. 2.

[23] Mishuris, G.S., Movchan, A.B., Slepyan, L.I., (2009): Localization and dynamic defects in lattice structures. Computational and Experimental Mechanics of Advanced Materials, CISM International Centre for Mechanical Sciences. Eds: P.D. Ruiz and V.V. Silberschmidt, Springer, 51–82.

[24] Mishuris, G.S., Movchan, A.B., Slepyan, L.I. (2009): Localised knife waves in a structured interface, Journal of the Mechanics and Physics of Solids 57, 1958–1979.

[25] Movchan, A.B., Brun, M., Slepyan, L.I., Giaccu, G.F., (2015): Dynamic multi-structure in modelling a transition flexural wave, Mathematika, Firstview, 2, 1-13, doi:10.1112/S0025579314000321.

[26] Nieves, M.J., Mishuris, G.S., Slepyan, L.I. (2016): Analysis of dynamic damage propagation in discrete beam structures, International Journal of Solids and Structures 97–98, 699-713.

[27] Nieves, M.J., Movchan, A.B., Jones, I.S., Mishuris, G.S. (2013): Propagation of Slepyan's crack in a non-uniform elastic lattice, Journal of the Mechanics and Physics of Solids 61, 1464-1488.

[28] Noble, B., (1958): Methods based on the Wiener-Hopf technique for the solution of partial differential equations. International Series of Monographs on Pure and Applied Mathematics 7, Pergamon Press, New York.

[29] Park, K. Paulino, G.H., Roesler, J. (2010): Cohesive fracture model for functionally graded fiber re-enforced concrete. Cement and Concrete Research 40, no. 6, 956–965.

[30] Quintana-Alonso, I and Fleck NA: (2010): Fracture of brittle lattices - a review. An anthology of ONR sponsored research, Springer, ed. EE Gdoutos.

[31] Rahulkumar, P., Jagota, A., Bennison, S.J., Saigal, S. (2000): Cohesive element modeling of viscoelastic fracture: application to peel testing of polymers. International Journal of Solids and Structures 37, no. 13, 1873–1897.

[32] Ryvkin, M. (2012): Analytical solution for a Mode III crack in a 3D beam lattice, International journal of Solids and Structures 49, 19–20, 2839–2847.

[33] Ryvkin, M., Slepyan, L., (2010): Crack in a 2D beam lattice: Analytical solutions for two bending modes, Journal of the Mechanics and Physics of Solids 58, 902–917.

[34] Slepyan, L.I., (2001): Feeding and dissipative waves in fracture and phase transition. I. Some 1D structures and a square-cell lattice, J. Mech. Phys. Solids 49, 469-511.

[35] Slepyan, L.I., (2001): Feeding and dissipative waves in fracture and phase transition. III. Triangular-cell lattice, Journal of the Mechanics and Physics of Solids 49, 2839–2875.

[36] Slepyan, L.I., (2002): Models and Phenomena in Fracture Mechanics. Springer, Berlin.

[37] Slepyan, L.I., Ayzenberg-Stepanenko, (2002): Some surprising phenomena in weak-bond fracture of a triangular lattice, Journal of the Mechanics and Physics of Solids 50, (2002), 1591–1625.

[38] Slepyan, L.I. and Ayzenberg-Stepanenko (2006): Crack dynamics in a nonlinear lattice, Int J Fract 140, 235–242.

[39] Slepyan, L.I., Ayzenberg-Stepanenko, M.V., and Mishuris, G.S., (2015). Forerunning mode transition in a continuous waveguide. J. Mech. Phys. Solids 78, 32-45. http://dx.doi.org/10.1016/j.jmps.2015.01.015

[40] Slepyan, L.I., and Troyankina, L.V., (1984): Fracture Wave in a Chain Structure. J. Appl. Mech. Techn. Phys., 25, No 6, 921-927.

[41] Siegmund, T., Brocks, W. (2000): A numerical study on the correlation between the work of separation and the dissipation rate in ductile fracture. Engineering Fracture Mechanics 67, no. 2, 139–154.

[42] Secchi, S., Simoni, L., Schreifler, B.A. (2004): Cohesive fracture growth in a thermoelastic bimaterial medium. Computers and Structures 82, no. 23–26, 1875–1887.